WEAKLY SUPERVISED DEEP REPRESENTATIONS FOR THE CHARACTERIZATION OF NANOSTRUCTURED METALLIC FOAMS FROM PORE GEOMETRICAL FEATURES.

WILLIAM DAVID ROMERO SERRANO

UNIVERSIDAD INDUSTRIAL DE SANTANDER
FACULTAD DE INGENIERÍAS FISICOMECÁNICAS
ESCUELA DE INGENIERÍA DE SISTEMAS E INFORMÁTICA
BUCARAMANGA
2025

WEAKLY SUPERVISED DEEP REPRESENTATIONS FOR THE CHARACTERIZATION OF NANOSTRUCTURED METALLIC FOAMS FROM PORE GEOMETRICAL FEATURES.

WILLIAM DAVID ROMERO SERRANO

Research work in partial fulfillment of the requirements for the degree of:
Magíster en Ingeniería de Sistemas e Informática

Advisor:
Fabio Martínez Carrillo
Ph.D in Systems and Computer Engineering

UNIVERSIDAD INDUSTRIAL DE SANTANDER
FACULTAD DE INGENIERÍAS FISICOMECÁNICAS
ESCUELA DE INGENIERÍA DE SISTEMAS E INFORMÁTICA
BUCARAMANGA
2025

ACKNOWLEDGMENTS

The author expresses his acknowledgment:

To God for giving me strength.

To my mother, whose unwavering dedication, boundless sacrifice, and quiet strength have shaped the very foundation upon which this work stands. Without her, none of this would hold meaning.

To my father and brother, for their presence and encouragement throughout this process.

To Emily, for being by my side, for coloring my life when it threatened to turn gray, for your patience that soothed my storms, your love that warmed my days, and your trust that gave me the courage to carry on.

To Professor Fabio, for being such a mentor. Your guidance, wisdom, and sincere dedication not only fostered my academic and professional growth, but also taught me the invaluable lesson of striving for excellence in all facets of life.

To the $Bivl^2ab$ team: Aleja, Santi, Edguir, Andrés, Ferchis, Franklin, Guayin, Edward, Jean, and the whole gang. Thank you for lighting the way, for turning challenges into shared laughs, and for making this journey a far more joyful one.

To my family, for being the quiet strength behind every step I took, for offering their hands when I faltered. Without your support, this endeavor would not have been possible.

And to the Universidad Industrial de Santander and the Escuela de Ingeniería de Sistemas, for their financial support, without which this research could not have been pursued.

CONTENIDO

page

LISTA DE FIGURAS

page

LISTA DE TABLAS

page

LIST OF APPENDICES

page

ABSTRACT

TITLE: WEAKLY SUPERVISED DEEP REPRESENTATIONS FOR THE CHARACTERIZATION OF NANOSTRUCTURED METALLIC FOAMS FROM PORE GEOMETRICAL FEATURES. *

AUTHOR: WILLIAM DAVID ROMERO SERRANO **

KEYWORDS: POROUS METALS, ELECTROCHEMICAL DEPOSITION, NANOSTRUCTURED METALLIC FOAMS, SELF-SUPERVISED ARCHITECTURES, DEEP REPRESENTATIONS, DEEP LEARNING DISENTANGLEMENT, WEAKLY SUPERVISED LEARNING, PORE FEATURES.

DESCRIPTION: The Dynamic Hydrogen Bubble Template Electrodeposition Method (DHBT) is a versatile technique for synthesizing nanostructured metallic foams (MFs) with intricate porous architectures. Understanding the interplay between pore geometry and the mechanical and electrochemical properties of MFs is essential, yet traditional characterization methods still are labor-intensive, subjective, and prone to errors. In this research work, we proposed two computational approaches to support MFs characterization, which consider a set of synthesized bimetallic CuNi alloy foams with varying Cu/Ni ratios using the dynamic hydrogen bubble template method. This study considers a total of 923 micrographs of three different chemical compositions. The first approach segmented the porous structure of the foams and extracted a suite of basic shape descriptors for each image, including pore area distribution, pore perimeter distribution, equivalent diameter distribution and total pore count. We also computed pore size distribution and quantified the degree of mercury removal achieved by the synthesized Cu/Ni alloy foams. This approximation achieved an average segmentation capability of 91% and regarding classification an average precision and recall of 83% and 80%, respectively. Secondly, we introduced a disentangling approximation to automatically characterize metallic foams (MFs) by learning image features observed over micrographs, which are regularized with geometrical pore features such as area, perimeter, equivalent diameter, and the number of pores. The recovered MFs descriptor can classify MFs according to chemical composition, bringing support in the design of foams for dedicated applications. This approximation achieved an average precision and recall of 84% and 80%, respectively. Our findings reveal a significant correlation between the Cu/Ni ratio and the porous structure of the Cu/Ni foams. The proposed

---

* Research work

** Facultad de Ingeniería fisicomecánicas. Escuela de Ingeniería de Sistemas e Informática. Advisor: Fabio Martínez Carrillo, Ph.D.

method for pore shape analysis in metallic foams, providing valuable insights into the relationship between composition and morphology.

RESUMEN

TÍTULO: REPRESENTACIONES PROFUNDAS DÉBILMENTE SUPERVISADAS PARA LA CARACTERIZACIÓN DE ESPUMAS METÁLICAS NANOESTRUCTURADAS A PARTIR DE CARACTERÍSTICAS GEOMÉTRICAS DE PORO. *

AUTOR: WILLIAM DAVID ROMERO SERRANO **

PALABRAS CLAVE: METALES POROSOS, DEPOSICIÓN ELECTROQUÍMICA, ESPUMAS METÁLICAS NANOESTRUCTURADAS, ARQUITECTURAS AUTO-SUPERVISADAS, REPRESENTACIONES PROFUNDAS, EXPLICABILIDAD EN APRENDIZAJE PROFUNDO, APRENDIZAJE DÉBILMENTE SUPERVISADO, CARACTERÍSTICAS DE LOS POROS.

DESCRIPCIÓN: El método de electrodeposición con plantilla dinámica de burbujas de hidrógeno (DHBT, por sus siglas en inglés) es una técnica versátil para la síntesis de espumas metálicas (MFs) nanoestructuradas con arquitecturas porosas complejas. Comprender la relación entre la geometría de los poros y las propiedades mecánicas y electroquímicas de estas espumas es esencial. Sin embargo, los métodos tradicionales de caracterización siguen siendo laboriosos, subjetivos y propensos a errores. En este trabajo de investigación, se propusieron dos enfoques computacionales para apoyar la caracterización de MFs. Estos métodos se probaron en un conjunto de espumas bimetálicas de aleación Cu-Ni con diferentes proporciones Cu/Ni sintetizadas mediante DHBT, analizando un total de 923 micrografías de tres composiciones químicas distintas. El primer enfoque segmentó la estructura porosa de las espumas y extrajo descriptores básicos de forma, como la distribución del área y perímetro de los poros, el diámetro equivalente y el recuento total de poros. También se analizó la distribución del tamaño de los poros y se cuantificó la capacidad de las espumas CuNi para eliminar mercurio, logrando una capacidad de segmentación promedio del 91% y una precisión y exhaustividad promedio del 83% y 80%, respectivamente. El segundo enfoque introdujo una aproximación basada en desentrelazamiento de propiedades para caracterizar automáticamente las espumas metálicas a partir de características observadas en las micrografías, regularizadas con atributos geométricos de los poros. Este descriptor permitió clasificar las espumas según su composición química, logrando una precisión y exhaus-

---

* Trabajo de investigación

** Facultad de Ingeniería Fisicomecánicas. Escuela de Ingeniería de Sistemas e Informática. Director: Fabio Martínez Carrillo, Ph.D.

tividad promedio del 84% y 80%, respectivamente. Los resultados revelan una correlación significativa entre la proporción Cu/Ni y la estructura porosa de las espumas Cu/Ni, proporcionando herramientas valiosas para diseñar espumas con aplicaciones específicas y relacionar composición y morfología.

INTRODUCTION

Nanostructured metallic foams (MFs) produced via the dynamic hydrogen bubble template (DHBT) electrodeposition method exhibit a wide range of properties, tunable through precise control over the deposition process [1] [2] [3] [4]. The intricate interplay between the dynamics of hydrogen bubble formation and the deposition process results in materials with tailored properties, such as enhanced surface area and controlled pore size distributions [1]. Properties such as the electrical conductivity and mechanical strength of MFs are influenced by their porosity and pore geometry. Larger, well-connected pores facilitate electron transport, which provides electrical conductivity, whereas smaller, isolated pores can hinder it [5]. The mechanical strength of foams is impacted by their porosity, with a higher number of pores increasing the susceptibility to fracture propagation, leading to reduced mechanical integrity [6]. This interplay between electrical conductivity and mechanical strength highlights the importance of tuning porosity for specific applications.

---

[1] Xurui MA et al. "Research and development progress of porous foam-based electrodes in advanced electrochemical energy storage devices: A critical review". In: *Renewable and Sustainable Energy Reviews* 173 (2023), p. 113111.

[2] Oxana Vasilievna KHARISSOVA; Leticia Myriam TORRES-MARTÍNEZ, and Boris Ildusovich KHARISOV. *Handbook of nanomaterials and nanocomposites for energy and environmental applications*. Springer, 2021.

[3] DoHwan NAM et al. "Effects of (NH4) 2SO4 and BTA on the nanostructure of copper foam prepared by electrodeposition". In: *Electrochimica Acta* 56.25 (2011), pp. 9397–9405.

[4] H-C SHIN; Jian DONG, and Meilin LIU. "Nanoporous structures prepared by an electrochemical deposition process". In: *Advanced Materials* 15.19 (2003), pp. 1610–1614.

[5] BQ LI and X LU. "The effect of pore structure on the electrical conductivity of Ti". In: *Transport in Porous Media* 87.1 (2011), pp. 179–189.

[6] P ARÉVALO-CID; MF VAZ, and MF MONTEMOR. "Highly porous FeNi 3D foams produced by one-step electrodeposition: Electrochemical stability and mechanical properties". In: *Materials Characterization* 193 (2022), p. 112311.

Consequently, a thorough understanding of the relationship between pore geometry and the resulting material properties is crucial for optimizing their performance in diverse kinds of applications such as catalysis and energy storage[1] [2] [7]. Traditional methods for characterizing porous materials rely on manual image analysis, involving the tedious and subjective task of annotating pore features from microscopy images. This approach is inherently prone to human error and can be time-consuming, hindering efficient and reliable assessment of the complex pore structures and their impact on material properties [8]. This limitation underscores the need for more reliable and efficient techniques to accurately assess the complex pore structures and their impact on the mechanical and electrochemical properties of metallic foams. Recent advancements in deep learning have offered promising alternatives for the automated analysis of porous materials [9]. Convolutional neural networks (CNNs) have successfully identified complex pore structures in various materials, including polymeric foams [10]. However, existing methods cannot often generate robust, interpretable descriptors that capture the intricate relationship between pore geometry and material properties.

This research work introduces two computational approaches dedicated to the characterization of MFs, considering synthesized bimetallic Cu/Ni alloy foams with varying Cu/Ni ratios. Firstly, we introduce a method for analyzing the shape of pores in top-view images, using a U-Net architecture for image segmentation, which offers a comprehensive and efficient approach for quantitatively characterizing the pore structures in these foams. Extracting pore geometrical features from the segmented images enables us to construct statistical distribu-

---

[7] Soma VESZTERGOM et al. “Hydrogen bubble templated metal foams as efficient catalysts of CO2 electroreduction”. In: *ChemCatChem* 13.4 (2021), pp. 1039–1058.

[8] Benoit HILLOULIN et al. “Modular deep learning segmentation algorithm for concrete microscopic images”. In: *Construction and Building Materials* 349 (Sept. 2022). DOI: 10.1016/j.conbuildmat.2022.128736.

[9] Ying DA WANG et al. “Deep learning in pore scale imaging and modeling”. In: *Earth-Science Reviews* 215 (2021), p. 103555.

[10] Jorge TORRE et al. “On the use of neural networks for the structural characterization of polymeric porous materials”. In: *Polymer* 291 (Jan. 2024). DOI: 10.1016/j.polymer.2023.126597.

tions for different classes of MFs. We also employ supervised learning with the extracted features to classify and discriminate between different foam types. Furthermore, we evaluate the application of this method to determine the extent of mercury removal over the synthesized Cu/Ni alloy foams. Secondly, we introduce a novel approach that integrates a variational autoencoder (VAE) to learn a latent representation of MFs that captures visual and geometric foam features. By incorporating specific pore geometrical features (e.g., area, perimeter, and equivalent diameter) into the training process, we enable the model to generate a latent space that effectively discriminates between different classes of foams based on their structural characteristics. Furthermore, we introduce a discriminative component to enhance the model's ability to reconstruct input images and disentangle the underlying factors of variation in the data. Our results demonstrate that the proposed approach can effectively characterize MFs and generate robust, interpretable representations of their pore structures. The model's ability to accurately classify foams based on their geometric features highlights its potential for materials design.

1. Cu/Ni FOAMS AND POROUS MATERIAL CHARACTERIZATION

Cu/Ni nanostructured metallic foams are low-cost highly porous materials with properties such as low density, and good electrical conductivity that make them suitable for diverse applications, ranging from electrocatalysis to advanced materials engineering[11] [12] [13] [14]. The dynamic hydrogen bubble template (DHBT) method has emerged as a promising technique for synthesizing foams with open porous structures that exhibit desirable properties for various applications[11] [15]. This electrochemical method hinges on the hydrogen bubbles generation in an aqueous solution containing conventionally one or two metallic precursors[7]. The hydrogen bubbles grow and rupture, leaving a cellular structure of metal or alloy deposited on a metal substrate. DHBT-synthesized metallic foams possess properties and functionalities highly dependent on their pore structure[11] [15] [7]. The synthesis process is illustrated in Figure 1.

---

[11] Farhan ARSHAD et al. "Bubbles Templated Interconnected Porous Metallic Materials: Synthesis, Surface Modification, and their Electrocatalytic Applications for Water Splitting and Alcohols Oxidation". In: *ChemistrySelect* 7.41 (2022), e202202774.

[12] O SURUCU. "Electrochemical removal and simultaneous sensing of mercury with inductively coupled plasma-mass spectrometry from drinking water". In: *Materials Today Chemistry* 23 (2022), p. 100639.

[13] Thien-Khanh TRAN et al. "Electrochemical treatment of wastewater: Selectivity of the heavy metals removal process". In: *International Journal of hydrogen energy* 42.45 (2017), pp. 27741–27748.

[14] Mattias KO BENGTSSON; Cristian TUNSU, and Bjorn WICKMAN. "Decontamination of mercury-containing aqueous streams by electrochemical alloy formation on copper". In: *Industrial & Engineering Chemistry Research* 58.21 (2019), pp. 9166–9172.

[15] Manisha DAS et al. "The versatility of the dynamic hydrogen bubble template derived copper foam on the emerging energy applications: progress and future prospects". In: *Journal of Materials Chemistry A* 10.26 (2022), pp. 13589–13624.

Figure 1. Schematic illustration of nanofoam synthesis by the dynamic hydrogen template method. Adapted from Plowman et al [16].

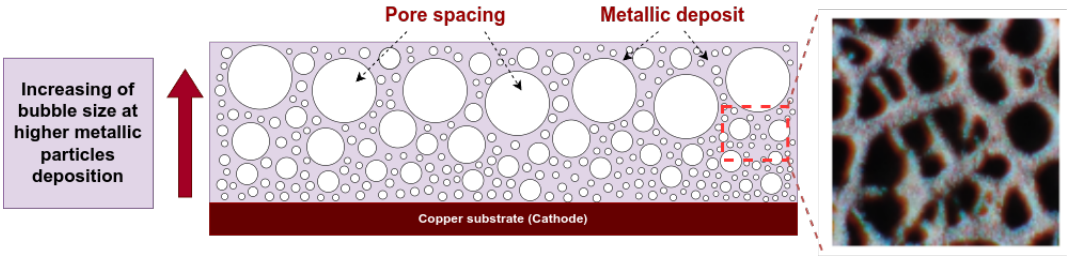

The synthesis process of these metallic foams (MFs) is shown in Figure 2. For a more detailed visualization, refer to the accompanying video: **Synthesis of Cu/Ni Metallic Foams**.

Figure 2. Synthesis process and top-view visualization of MFs using the DHBT method

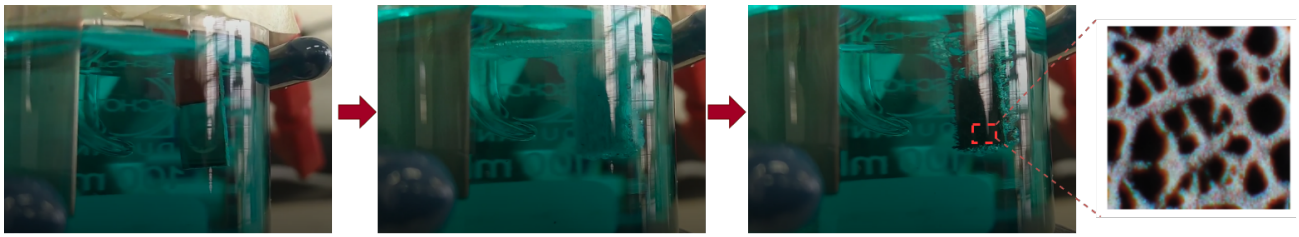

The analysis of foams and porous materials in general rely on manual image analysis, where experts observe the images, take measures, and approximate distributions of geometric properties to conclude about synthesized materials. Nonetheless, these analyses are tedious and subjective, involving the delineation of pores and the measure of geometric features from microscopy images. Of course, this approach is biased, inherently prone to human error and can be time-consuming, hindering efficient and reliable assessment of the complex pore structures and their impact on material properties [8].

Recent computational advancements have emerged as a promising alternative to support the analysis and characterization of materials, achieving comparable or even superior results[9]. Particularly, convolutional neural networks (CNNs) are a cornerstone of deep learning

and excel at image segmentation tasks[17], extracting features to quantify various properties of porous materials based on their geometric characteristics. Building on cross-sectional photographs, Zhou et al.[18] introduced DeepLabV3+ model, an encoder-decoder scheme based on the Xception architecture to analyze pore size distribution in scanning electron microscopy (SEM) images. Such approach segments pores larger than 10 µm, significantly reducing the time required for image analysis but requiring some preprocessing such as the cutting and polishing of concrete samples. Similarly, Torre et al.[19] adapted Mask R-CNN models for the automatic characterization of porous polymeric materials, using SEM microscopic images of materials like extruded polystyrene (XPS), polyurethane (PU), and poly(methyl methacrylate) (PMMA), as well as open-pore PU, capturing the structural features of different polymers. In another study, Karaca et al.[20] introduced Pore D2 (an adaptation of Yolov5), a net dedicated to detect pore and window sizes in SEM images of open-porous scaffolds. These computational approximations have evidenced remarked performance on the detection and quantification of pores, being required new proposals dedicated to segment objects to capture local details of pores, which are fundamental in geometrical analysis. The U-Net model is a deep learning architecture specifically designed for semantic segmentation. Its encoder-decoder structure facilitates comprehensive sampling by merging low-resolution information for object classification with high-resolution details for precise segmentation. Originally developed

---

[17] Laith ALZUBAIDI et al. "Review of deep learning: concepts, CNN architectures, challenges, applications, future directions". In: *Journal of big Data* 8 (2021), pp. 1–74.

[18] Shuangxi ZHOU et al. "Quick image analysis of concrete pore structure based on deep learning". In: *Construction and Building Materials* 208 (May 2019), pp. 144–157. DOI: 10.1016/J.CONBUILDMAT.2019.03.006.

[19] Jorge TORRE et al. "On the use of neural networks for the structural characterization of polymeric porous materials". In: *Polymer* 291 (2024), p. 126597.

[20] Ilayda KARACA and Betul ALDEMIR DIKICI. "Quantitative Evaluation of the Pore and Window Sizes of Tissue Engineering Scaffolds on Scanning Electron Microscope Images Using Deep Learning". In: *ACS Omega* (2024).

for medical imaging, U-Net is highly effective at delineating complex boundaries and has established itself as a foundational model across multiple disciplines. Its exceptional performance renders it particularly well-suited for accurately segmenting intricate geometries, such as pore structures within metallic foams[21] [9]. However, while these approaches excel in analyzing material structures, they lack computational mechanisms to describe complex structures as coding robust descriptors that summarize material configurations. To overcome this limitation, Zhu et al.[22] introduced a generative framework that combines a residual convolutional neural network with an improved Monte Carlo search to identify complex textural patterns to design optimal surface textures, tailored to specific tribological requirements. Also, Variational Autoencoders (VAEs) and Generative Adversarial Networks (GANs) have been proposed to generate new material designs, enabling better exploration and assessment of tailored physical features distributions[23]. In such line, Gómez-Bombarelli et al.[24] proposed a method using a variational autoencoder (VAE) to map molecular structures into a continuous latent space, enabling efficient gradient-based optimization to generate molecular structures through latent space manipulations such as decoding random vectors, modifying existing molecules, or interpolating between known compounds.

Disentanglement methodologies Generative deep learning architectures such as autoencoders aim for coding visual characteristics of input data into features descriptors (z). Figure 3 shows a latent space generated from MFs embedded descriptors using a deep con-

---

[21] R ARCHANA and PS Eliahim JEEVARAJ. "Deep learning models for digital image processing: a review". In: *Artificial Intelligence Review* 57.1 (2024), p. 11.

[22] Bao ZHU et al. "Generative design of texture for sliding surface based on machine learning". In: *Tribology International* 179 (2023), p. 108139.

[23] Teng LONG; Yixuan ZHANG, and Hongbin ZHANG. "Generative deep learning for the inverse design of materials". In: *arXiv preprint arXiv:2409.19124* (2024).

[24] Rafael GÓMEZ-BOMBARELLI et al. "Automatic chemical design using a data-driven continuous representation of molecules". In: *ACS central science* 4.2 (2018), pp. 268–276.

volutional neural network. These descriptors encode textural, geometric, and color features of input images, allowing them to represent information in a low-dimensional space. From this low-dimensional space it is possible to visualize cloud of points that represent complex structures and to support observational analysis, for instance, to determine properties of certain materials according to neighborhoods. Hence, this computational representations are an opportunity to improve MFs characterization using deep learning models, allowing us to correlate the feature descriptors to specific pore geometrical characteristics.

Figure 3. Latent space from MFs' micrograph generated by a convolutional deep neural architecture

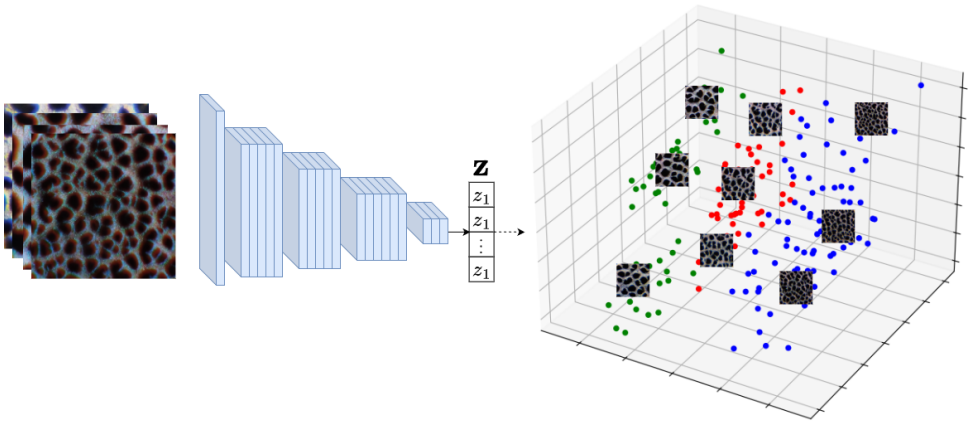

However, there still a gap on learning interpretable latent space for this descriptors from input data using this kind of architectures[25]. Therefore, there have been developed several methods to achieved such interpretability, for example, Liu et al.[26] proposed a disentanglement algorithm to visually explain VAES results, where each element within the latent vector can be explained individually by attention maps. In their work they presented a modification in the loss function of a one-class VAE to infuse the attention maps into the training process. Thus,

---

[25] Zheng DING et al. "Guided variational autoencoder for disentanglement learning". In: *Proceedings of the IEEE/CVF conference on computer vision and pattern recognition*. 2020, pp. 7920–7929.

[26] Wenqian LIU et al. "Towards visually explaining variational autoencoders". In: *Proceedings of the IEEE/CVF Conference on Computer Vision and Pattern Recognition*. 2020, pp. 8642–8651.

improving latent space explainability of embedded vectors components when an anomaly image is passed through the network. However, they did not correlate each component of the latent space to a unique visual characteristic on the images. Harkness et al.[27] presented an approach to disentangled latent space representations for multi-label classification of chest x-ray (CXR) images. As each class of CXR images present specific visual clinical-relevant characteristics, they proposed a VAE to code those characteristic into embedded vectors. Then, they implemented an explainability method to highlight the most relevant regions in the images per each class. Also, they showed that under their methodology it is possible to modify the clinical-relevant characteristics of the images from one class to another by modifying the values of specific components in the embedded vectors. However, as far as we know, there are not previous works related to disentangling of latent space using deep learning approaches for MFs characterization.

Computational approaches to characterize materials by quantification of pore geometrical properties have been made in order to avoid observation bias and reducing cost associated to porous materials synthesis. For example, Chung et al.[28] used X-ray micro-computed tomography (micro-CT) imaging for the estimation of mechanical properties of foamed material samples. They captured descriptors for assessing pore circularity and relative density based on binarized images of the material, and then, corroborating the reliability of these descriptors through experimental validation. Liu et al.[29] showed and existing connection between the geometrical pore parameters and the mechanical attributes of MFs by analyzing geometric features within binarized images acquired from a scanning electron microscope (SEM).

---

[27] Rachael HARKNESS et al. “Learning disentangled representations for explainable chest X-ray classification using Dirichlet VAEs”. In: *arXiv preprint arXiv:2302.02979* (2023).

[28] Sang Yeop CHUNG et al. “Pore characteristics and their effects on the material properties of foamed concrete evaluated using micro-CT images and numerical approaches”. In: *Applied Sciences* 7.6 (2017), p. 550.

[29] Ran LIU and Antonia ANTONIOU. “A relationship between the geometrical structure of a nanoporous metal foam and its modulus”. In: *Acta Materialia* 61.7 (2013), pp. 2390–2402.

Romero et al.[30] introduced a geometrical characterization of MFs using a convolutonal variational autoencoder (VAE). In their research, they employed grad-cam maps to highlight the most relevant areas within MFs confocal images regarding each embedded vector component. Despite achieving classification accuracy above 90%, it remained uncertain which particular geometrical property corresponded to each component of the embedded vectors. This limitation remarks the challenge of disentangling the latent space.

[30] William D ROMERO et al. “Geometrical Recognition of Metallic Foam Microstructures Using a Deep Learning Approach”. In: *Available at SSRN 4564423* ().

2. RESEARCH PROBLEM

Nanostructured metallic foams have emerged as a potential class of materials with unique porous structures and properties such as high surface area, increased surface reactivity, and tunable morphology and composition. This unique set of attributes makes nanostructured metallic foams highly versatile materials with promising applications to absorb substances such as mercury from water. Nonetheless, the designs of these nanostructured metallic foams are principally based on trial-and-error methodologies that limit the exploration of mechanical and electrochemical properties.

Typically, the analysis of these mechanical and electrochemical properties is related to pore geometry distributions, observed from microscopical observations. However, this analysis is based on the recovery of geometrical distributions from observed samples, which may be a tedious procedure, time-consuming, and even human-biased because of the annotations of the observed samples. Nowadays, there is evidence in the literature of computational support to carry out such analysis, measuring geometric primitives from observations, using image analysis descriptors. These descriptors however may limit the description of the morphology in nanostructured metallic foams, losing hidden information that may supports mechanical and electrochemical properties. Also, other approaches have implemented machine-learning strategies to learn material structure distribution, but following strict supervision from labeled samples, which in turn difficult the generalization to other applications and analyses. Today, alternative computational schemes that code microstructure properties correlated with the efficiency of electrochemical reactions and convective-diffusive mass transport are demanded. Also, these strategies are desirable to be self-explained to support expert decisions about the capability of observed materials, as well as, the discriminating character among different mechanical properties, and material compositions.

Research Question

Considering these statements, we propose to address the following research question:

- How to disentangle embedding pore geometrical features from nanostructured metallic foam observations?

From such research question the next two question can be extracted:

- How pore geometrical characteristics can be extracted from nanostructured metallic foam observations?
- How to include pore geometrical characteristics into model training?

Hypothesis

According to the identified research problem and the established research questions, the next hypothesis was formulated:

- Including pore geometrical features into model training can disentangle the embedding space of nanostructured metallic foam observations regarding pore geometrical features

3. OBJECTIVES

General Objective

- To propose a weakly supervised model that include embedding disentangle strategies to characterize pore geometrical features.

Specific Objectives

- To prepare a dataset of nanostructured metallic foams with the corresponding pore geometrical features.
- To design a deep learning architecture to encode structural features of nanostructured metallic foams micrographs.
- To integrate pore geometrical features into the learning strategy from an end-to-end scheme.
- To validate the discriminant capability of recovered embedding descriptors regarding geometrical and composition features.

4. AUTOMATIC PORE SHAPE CHARACTERIZATION IN METAL FOAMS TEMPLATED BY HYDROGEN BUBBLES FROM A DEEP LEARNING STRATEGY

This study introduces a computational framework to automatically characterize pore geometrical features and classify three distinct types of MFs from micrographs. Firstly, a deep U-net architecture is automatically adjusted to segment pores from MFs' observations. Then, each pore retrieved from the segmentation map is individually characterized regarding the pore perimeter, area, and equivalent diameter. Subsequently, statistical descriptors are built to summarize MFs' observations by aggregating the features retrieved from each pore in the image. These descriptors allow the classification of MF samples according to their chemical composition based on the geometry of pore features, opening the opportunity to discover and emulate new MF compositions related to those specific pore features. The general pipeline of the proposed framework is illustrated in Figure 4. A partial content of this work has been accepted and published as **Romero, W. D., Gutierrez, Y., Tami-Pimiento, L. M., Torres-Bermudez, S., Meléndez, A. M., & Martínez, F. (2024). Automatic pore shape characterization in metal foams templated by hydrogen bubbles from a deep learning strategy. Materials Today Communications, 41, 110937.**

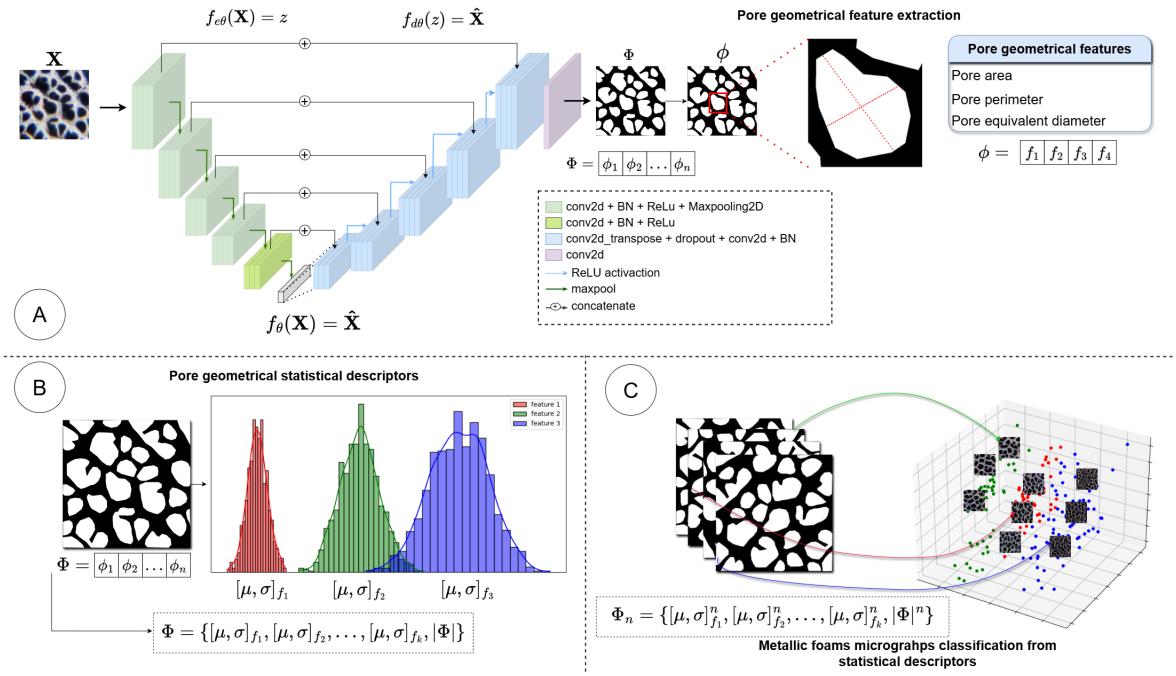

Figure 4. Deep learning for characterization of metallic foams (MFs). A) A U-Net model segments pores in MF micrographs. Extracted features include pore area, perimeter, and equivalent diameter. B) A set of statistical descriptors for these features and pore count represents each image. C) Pore geometry descriptors are used to classify MF images based on chemical composition using machine learning (decision tree, random forest, support vector machine).

4.1. Pore segmentation from a deep representation

MF analysis lies in the individual pore characterization to ascertain the chemical composition of porous materials. We undertake pore segmentation of MF images by employing a deep learning strategy, following supervised training with images annotated by experts. We adapted a U-net deep architecture (f_θ) coded with an encoder and decoder processing paths. This architecture (f_θ) learns θ parameters, being the encoder $(f_{e\theta}(\mathbf{X}) = z)$ responsible to downsamples input images $\mathbf{X}$ through series of convolutional and pooling layers, capturing contextual information into low-dimensional representations called embedded vectors (z). The decoder $(f_{d\theta}(z) = \hat{\mathbf{X}})$ processes the embedded vectors of the encoder through a series of convolutional layers to spatially localize the features and brings back high-resolution infor-

mation [31]. The skip-connections are architectural elements of the U-net model that establish links between layers in the encoder and their corresponding counterparts in the decoder. To achieve this, feature maps of the encoder are concatenated with the corresponding feature maps at the same spatial level in the decoder. This concatenation enables the decoder to access information from encoder processing, preserving spatial patterns, and enhancing the model's ability to accurately segment and localize objects in the input image. This capacity to localize specific objects in images is crucial for pore identification and feature quantification over MFs' micrographs. The pore geometrical characterization of materials typically involves a manual process in which experts annotate pores and measure their properties tending to be prone to errors and time-consuming processes. In this context, this study introduces a U-Net model trained for the automatic segmentation and characterization of pores attributes in micrographs of MFs. The U-net model receives a grey-scale micrograph and turns it into a binarized image Φ that discriminates between pore and interstice area due to the segmentation task. Hence, each micrograph $\Phi = \{\phi_1, \phi_2, \phi_3, ..., \phi_n\}$ is a map of independent pores ϕ, where n is the number of pores per image.

4.2. Pore geometrical features and statistical descriptors

A MF micrograph analysis is fully based on a statistical description of pore shape features. So, a principal characterization task consists of the measure of geometrical features of each identified pore ϕ, from automatic segmentation. Four geometrical pore features were selected to characterize each image observation in the dataset, defined as follows:

- The pore area (f_1) is defined as the cumulative number of pixels classified as pores within an MF's image. Each pixel has an approximated area of $\sim 1\mu m^2$

---

[31] Olaf RONNEBERGER; Philipp FISCHER, and Thomas BROX. "U-net: Convolutional networks for biomedical image segmentation". In: *Medical Image Computing and Computer-Assisted Intervention–MICCAI 2015: 18th International Conference, Munich, Germany, October 5-9, 2015, Proceedings, Part III 18*. Springer. 2015, pp. 234–241.

- The perimeter of a pore (f_2) is the number of pixels that enclose a detected pore shape.
- Equivalent diameter of a pore (f_3) denotes the diameter of a circle whose area matches that of the pore. To compute this measure, we circumscribe a circle around each detected pore and then measure the respective diameter.
- Cardinality of pores f_4 computed automatically from Φ

In such line, each pore is described by the four geometrical features, as $\phi_n = \{f_{k_1,n}, f_{k_2,n}, ..., f_{5,n}\}$. Each binarized image Φ, with n pores, is summarized as the set of normal distributions for each computed feature. In brief, each micrograph observation is described as the descriptor: $\{(\mathcal{N}\mu_{f_1}, \sigma^2_{f_1}), \mathcal{N}(\mu_{f_2}, \sigma^2_{f_2}), \ldots, \mathcal{N}(\mu_{f_5}, \sigma^2_{f_5}), |\phi|\}$ (see Figure 4).

From micrograph descriptors, it is possible to adjust machine learning algorithms with the capability to detect the chemical composition of NFM according to pore description. In such cases, we adjust computational strategies to predict the composition from the input of the signature Φ. In this work, we explore decision tree, random forest, and support vector machine classifiers. These classifiers are characterized by the capability to adjust boundaries from a few data samples and classify new MF samples. Also, we built a normal distribution of micrograph descriptors as an extra analysis tool to determine the discrimination of composition of materials from geometrical features, as typically carried out in the laboratory[32]. Thereby, pore feature distribution per class is built by aggregating individual features of MFs' observations to form Gaussian distributions for each pore feature $\mathcal{N}(\mu_k, \sigma^2_k)$. Subsequently, the probability $P(f_k|\mu_k, \sigma^2_k)$ of MFs' new samples to be part of a defined class is given by the normal density function for the pore feature mean and standard deviation.

---

[32] Yeonjoo PARK and Douglas G SIMPSON. "Robust probabilistic classification applicable to irregularly sampled functional data". In: *Computational statistics & data analysis* 131 (2019), pp. 37–49.

5. INTEGRATING PORE GEOMETRICAL FEATURES TO CHARACTERIZE NANOSTRUCTURED METALLIC FOAMS

An end-to-end disentanglement deep architecture is herein proposed to model digital low-dimensional descriptors of observed micrographs, which are discriminative according to the chemical composition. The architecture includes a multi-task learning, considering a variational autoencoder (VAE) to code the descriptor $\mathbf{z}$ from observed foam micrographs ($\mathbf{X}$). A discriminative adversarial encoder $h_\theta(\hat{\mathbf{X}}, \mathbf{X})$ is also included to force an effective pore reconstruction $\hat{\mathbf{X}}$. Besides, the proposed approach fine-tune geometrical descriptor $\mathbf{z}$ by projecting pore reconstruction $\hat{\mathbf{X}}$ to a decoder dedicated to predict pore geometrical features $\mathbf{F} = \{f_1, f_2, \ldots, f_k\}$. Through this dedicated learning process, the retrieved low-dimensional space demonstrate remarkable capabilities in classifying foams into three distinct compositional classes. An overview of the proposed pipeline is presented in Figure 5. The partial content of this work is under review as **Romero, W. D., Tami-Pimiento, L. M, Meléndez, A. M., & Martínez, F. (2025). Deep learning-driven integration of visual and geometric features for automated characterization of nanostructured metallic foams.**

Figure 5. Proposed weakly-supervised VAE framework for encoding pore geometrical features from metallic foam micrographs. The VAE compresses input micrographs into a latent space ($\mathbf{z}$), reconstructs them, and refines feature prediction with a regression module and discriminator. The learned embeddings enable micrograph classification by chemical composition, with insights provided through latent space visualization.

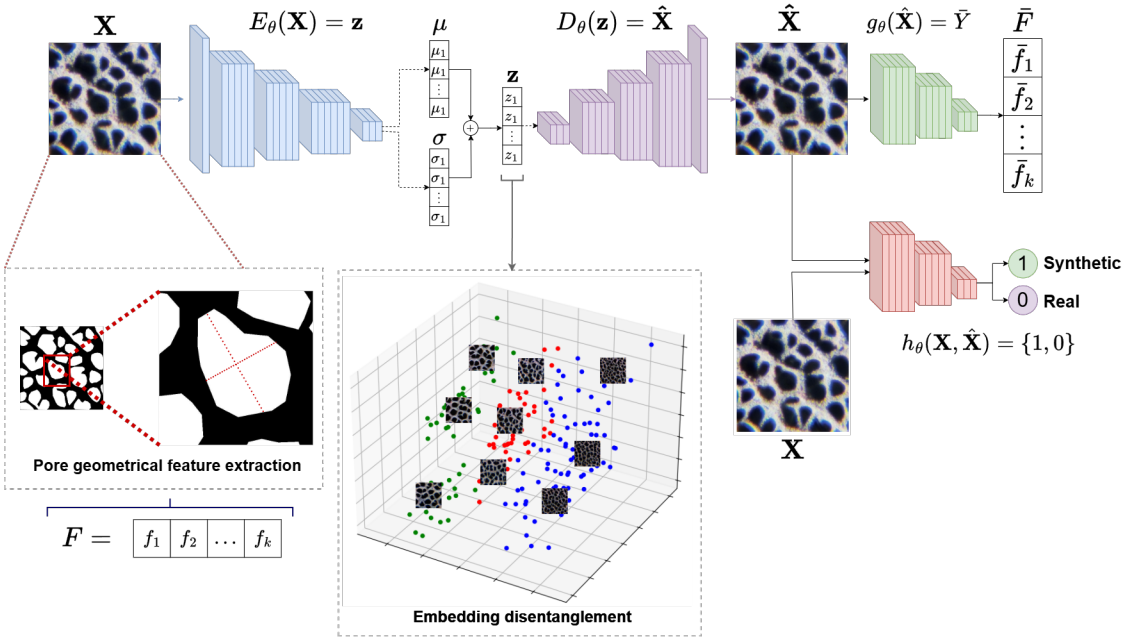

5.1. Variational Autoencoder for encoding a pore representation

The proposed approach includes a VAE architecture that learn a latent space, encoding each image as a set of normal distributions, parameterized by $\{\mu_i, \sigma_i\}_{i=1...k}$, following as a pretext task, the reconstruction of micrographs of metallic foams (MFs) [33] [34]. Particularly, the VAE was trained varying chemical compositions of input images $\mathbf{X}$, to retrieve a latent descriptor $\mathbf{z}$. These embedding descriptors summarize essential geometrical features of the

---

[33] Licheng JIAO and Jin ZHAO. "A Survey on the New Generation of Deep Learning in Image Processing". In: *IEEE Access* 7 (2019), pp. 172231–172263. DOI: 10.1109/ACCESS.2019.2956508.

[34] Diederik P KINGMA; Max WELLING, et al. "An introduction to variational autoencoders". In: *Foundations and Trends® in Machine Learning* 12.4 (2019), pp. 307–392.

foams, as Gaussian distributions. The decoder reconstructs the images $\bar{\mathbf{X}}$, using a binary cross-entropy reconstruction loss [35], expressed as:

$$R_{Loss} = -\frac{1}{M}\sum_{i=1}^{M}\sum_{j=1}^{n}[\mathbf{X}_{j,i} \cdot log(\bar{\mathbf{X}}_{j,i} + (1 - \mathbf{X}_{j,i}) \cdot log(1 - \bar{\mathbf{X}}_{j,i})] \tag{1}$$

VAE architecture is specifically tailored to ensure that the latent embeddings follow a standard Gaussian probabilistic distribution, represented as $\mathcal{N}(\mu = 0, \sigma = I)$. Enforcing this standard Gaussian distribution, we aim to learn smoother and consistent embeddings, following Kullback-Leibler divergence as [34] [36]:

$$KL_{loss} = -0.5 * \sum_{i=1}^{K}(1 + log(\sigma^2) - \mu^2 - \sigma^2) \tag{2}$$

It should be noted that the decoder accepts a one-dimensional vector for reconstructing the image $\bar{\mathbf{X}}$, allowing backpropagation of the error. Then, the 2D embedding vectors $\{\mu_i, \sigma_i\}_{i=1...k}$ are reparametrized by a linear that generates a unique one-dimensional sampling vector $\mathbf{z}$ [37] [38], expressed as $z = \mu + log(\sigma) * \epsilon \quad \forall\ \epsilon \in \mathcal{N}(0, I)$. Hence, the VAE follows a linear combination of both error terms, as $ELBO = KL_{Loss} + R_{Loss}$

The resultant VAE's latent space can be explored to identify material properties, and to find elements with similar mechanical characteristics, such as alloying levels that are useful in synthesizing MFs. Additionally, from such space, it is possible to digitally synthesize embeddings within this latent space that can simulate the formation and synthesis of new MFs

---

[35] Umberto MICHELUCCI. "An introduction to autoencoders". In: *arXiv preprint arXiv:2201.03898* (2022).

[36] Gregory P WAY and Casey S GREENE. "Extracting a biologically relevant latent space from cancer transcriptomes with variational autoencoders". In: *PACIFIC SYMPOSIUM on BIOCOMPUTING 2018: Proceedings of the Pacific Symposium*. World Scientific. 2018, pp. 80–91.

[37] Diederik P KINGMA and Max WELLING. "Auto-encoding variational bayes". In: *arXiv preprint arXiv:1312.6114* (2013).

[38] Carl DOERSCH. "Tutorial on variational autoencoders". In: *arXiv preprint arXiv:1606.05908* (2016).

[39].

5.2. A deep geometrical feature regressor

In this work, we introduced a complementary pretext task to aggregate specific pore features information that impact in the discrimination capability of the embedding space. Thus, it is expected to enhance the characterization of MFs during the end-to-end training process. These next features, were integrated to the VAE, and quantified from the micrograph masks: The complementary VAE adjusting from pore features was performed through pixel-wise measurements on the binary masks of metallic foam (MFs) images. This process embeds the key geometrical characteristics within the VAE's latent space, enhancing the ability to classify MFs based on chemical composition. Each input image $\mathbf{X}$ is paired with a hand-annotated mask $\mathbf{\Phi} = \{\phi_1, \phi_2, \ldots, \phi_n\}$, which maps individual pores ϕ across the image, where n represents the total number of pores. Each pore ϕ_n is described by a set of specific features $\{f_{1,n}, f_{2,n}, f_{3,n}\}$, summarized by the mean values of these computed features, resulting in a descriptor for each micrograph: $F = \{\mu_{f_1}, \mu_{f_2}, \mu_{f_3}, |\mathbf{\Phi}|\}$.

To enhance the embedding representation, an architecture extension aligns the latent representations with predefined pore geometrical features. Specifically, a convolutional neural network module, $(g_\theta(\bar{\mathbf{X}}) = \bar{\mathbf{F}})$, is incorporated into the VAE framework to predict the predefined geometrical descriptors $(\bar{\mathbf{F}})$ from the reconstructed images $(\hat{\mathbf{X}})$. To ensure the accurate encoding of these features, a mean squared error (MSE) loss is introduced between the predicted features $(\bar{\mathbf{F}})$ and the original features $(\mathbf{F})$, extracted from the binary mask. This additional loss term is integrated into the VAE's training process and is defined as $E_{loss} = \frac{1}{n}\sum_{1=1}^{n}(\mathbf{F_i} - \bar{\mathbf{F}}_\mathbf{i})^2$

---

[39] Christopher VOGELSANGER and Christian FEDERAU. "Latent space analysis of vae and intro-vae applied to 3-dimensional mr brain volumes of multiple sclerosis, leukoencephalopathy, and healthy patients". In: *arXiv preprint arXiv:2101.06772* (2021).

5.3. Adversarial Discriminator

The reconstruction performance of the Variational Autoencoder (VAE) was improved by integrating a CNN-based discriminator module ($h_\theta(\mathbf{X}, \hat{\mathbf{X}})$), following an adversarial rule that maximize the binary cross-entropy loss, penalizing missclassification of real samples as fake or generated samples as real, as follows:

$$D_{loss} = -\frac{1}{N}\sum_{i=1}^{N} log(D(\mathbf{X})) + log(1 - D(\hat{\mathbf{X}})) \tag{3}$$

Half of the data in each training batch, denoted as N, consist real samples, while the other half comprises generated samples. An optimal training is achieved when the discriminator can no longer distinguish between real and generated images, indicating that both have reached comparable quality. Thus, the complete proposed approach is adjusted as a combination of each introduced component as a linear combination of individual error terms presented previously, as follows $L_{total} = KL_{loss} + R_{loss} + E_{loss} + D_{loss}$.

5.4. MFs embeddings evaluation

Visualizing embedded vectors aids in recognizing patterns and understanding the distribution of properties within the latent space, However, it is equally important to evaluate how effectively the latent space separates different classes of vectors. Here, the separation was quantified using the following three clustering measures in this context:

Davies-Bouldin Index (DBI) quantifies similarity by the ratio of the average distance between points within the same cluster (intracluster distance) to the average distance between points in different clusters (inter-cluster distance). A lower DBI value indicates superior clustering performance. DBI is calculated as follows:

$$DB = \frac{1}{k}\sum_{i=1}^{k} max\left(\frac{\Delta(C_i)+\Delta(C_j)}{\delta(C_i,C_j)}\right) \tag{4}$$

Where k is the number of clusters, $\Delta(C_k)$ is the average intracluster distance within the cluster C_k and $\delta(C_i, Cj)$ is the average inter-cluster distances between clusters C_i and C_j.

Silhouette coefficient (SC) is a metric that combines cohesion (how close points are within a cluster) and separation (how far a point is from points in other clusters). This coefficient ranges from -1 to 1, where the higher the coefficient, the better the clustering performance, and a value of 0 indicates overlapping clustering. This metric is calculated as an individual coefficient S_k per cluster k, $WCSS_k$ is the within-cluster square separation and $BCSS_k$ is the between-cluster square separation to the closer cluster to cluster i, $|C_k|$ is the amount of data points in the cluster k, and $d(k, j)$ is the squared distance between k and j points inside the same cluster and $BCSS_k$ is the mean square distance from all the data point in cluster k to the centroid of a second cluster j. $S_k, WCSS_k$ and $BCSS_k$ are formulated as follows:

$$S_k = \frac{BCSS_k - WCSS_k}{\max(BCSS_k - WCSS_k)}, \quad BCSS_k = \min\left(\frac{1}{|C_j|}\sum_{k\in C_k} d(k,j)\right), \quad WCSS_k = \frac{1}{|C_k|-1}\sum_{k\in C_k, k\neq j} d(k,j)$$

Each, S_k is the relation of cohesion and separation between two cluster, however, when there are more than two clusters, we take the average coefficient S_k among clusters as the silhouette coefficient SC for all the dataset of points, as denoted $SC = \frac{1}{|C|}\sum_{i=1}^{|C|} S_i$, where $|C|$ is the number of clusters in the dataset.

Calinski-Harabasz Index (Variance Ratio Criterion (VRC)) measures the ratio the dispersion between cluster centroids and the global centroid of the dataset regarding the dispersion within each cluster, as follows:

$$CH = \frac{BCSS/(K-1)}{WCSS/(N-K)} \tag{5}$$

Where $BCSS$ is the sum of squares between groups $BCSS = \sum_{i=1}^{K} n_i \|\mathbf{C}_i - \mathbf{C}\|$, and $WCSS$ is the dispersion within each group $WCSS = \sum_{i=1}^{K} \sum_{\mathbf{x} \in \mathbf{C_i}} \|\mathbf{x} - \mathbf{c}_i\|$. The total number of clusters, n_i is the number of observations associated with the centroid C_i in the cluster i, and N is the total number of observations in the dataset. A higher index value indicates better clustering, with well-separated and compact clusters. This metric helps assess the degree of grouping in a dataset, with higher values reflecting more distinct and cohesive clusters.

6. EXPERIMENTAL SETUP

6.1. Data

All chemicals used in this study were of analytical grade and used as received without further purification. Copper(II) sulfate pentahydrate ($CuSO_4 \cdot 5H_2O$), nickel(II) sulfate hexahydrate ($NiSO_4 \cdot 6H_2O$), and sulfuric acid (H_2SO_4) were purchased from Sigma-Aldrich. Three distinct copper-nickel foams (MF1, MF2, and MF3) were synthesized via the DHBT electrodeposition method. The electrolyte solutions, each containing 1.5 M H_2SO_4, varied in the concentrations of $CuSO_4 \cdot 5H_2O$ and $NiSO_4 \cdot 6H_2O$ while maintaining a constant total metal ion concentration of 0.4 mol/L. The molar ratios of Cu^{2+} to Ni^{2+} in the electrolytes were 3:1, 1.67:1, and 1:1 for MF1, MF2, and MF3, respectively. Electrodeposition was conducted in a single-compartment electrochemical cell at room temperature using a potentiostat (PGSTAT302N, Metrohm Autolab). A copper plate (1.0 cm^2) served as the working electrode, while a copper foil and an Ag/AgCl (3 M KCl) electrode were used as the counter and reference electrodes, respectively. A constant current density of 3.0 A cm^{-2} was applied for 20 seconds for all depositions.

For each class, seven foam samples were analyzed. Micrographs of each foam were acquired using a portable microscope with 50x magnification, enabling detailed observation of the microstructures at the micron scale. An average of 50 images were captured per foam, ensuring comprehensive morphological coverage of each sample. To capture the inherent heterogeneity of the foam structures, images were acquired systematically across the surface of each sample using a grid pattern. This resulted in a total of 378, 284, and 261 images for MF1, MF2, and MF3, respectively. Each digitized image had a resolution of 1780 × 1780 pixels. Pores were annotated by experts to create a gold-standard reference for geometrical features, enabling the validation of the proposed method (Figure 6). Key geometrical features, including mean pore area, perimeter, and equivalent diameter, were extracted from

these annotations. Additionally, the total number of pores identified within each image was recorded.

Figure 6. Typical microscopic images of electrodeposited metallic foams (MFs) for each electrolyte composition (top) and their corresponding manually segmented pore structures (bottom). Electrolyte compositions (in molarity) are indicated in the figure.

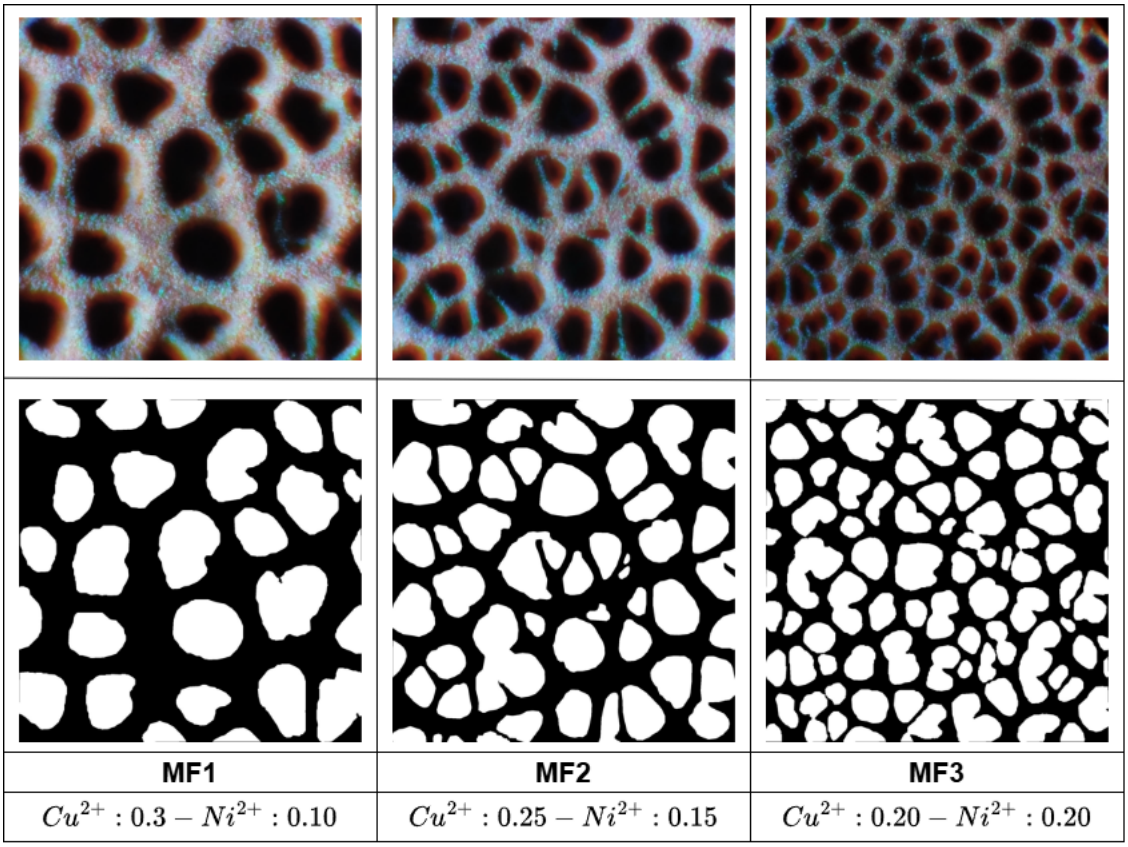

MF1	MF2	MF3
$Cu^{2+}: 0.3 - Ni^{2+}: 0.10$	$Cu^{2+}: 0.25 - Ni^{2+}: 0.15$	$Cu^{2+}: 0.20 - Ni^{2+}: 0.20$

6.2. Automatic pore shape characterization in MFs

The proposed approach was validated according to the capability to segment pores from micrographs images, and also regarding the capability to classify MF composition from geometrical pore features. For experimental validation, the methodology was adjusted, as:

- **Segmentation architecture.** The proposed architecture receives 128×128 images which are coded with five convolutional blocks in the segmentation dedicated net.

The first four blocks have a sequential combination of five convolutional layers with 16,32,64,128 and 256 filters, respectively. The decoder symmetrically has five transposed convolutional layers. The last layer was dedicated to recovering segmentation mask images with a dimension of 128×128. For the end-to-end training, the Adam optimizer was implemented with a learning rate of 0.0001, during 230 epochs, and a batch size of 512 images.

- **Geometrical descriptors.** Once the segmentation masks were retrieved, each pore was characterized by the area, perimeter, equivalent diameter, and number of pores. A Kolmogorov-Smirnov statistical test was run to observe statistical differences among MFs' compositions, following the characterization of pore features. Also, these features were used as descriptors to carry out an automatic classification. In such cases, a random forest (max-leaf nodes = 3, max depth = 5), a decision tree (max depth = 5), and a SVM (linear kernel) were implemented.

- **Data split.** For validation of the proposed approach, we implemented a five-fold cross-validation. In such case, the MFs dataset was split into five different folds where 80% of the data is used for training and 20% for testing. To evaluate the performance of the pore segmentation task, we employed metrics such as Dice score, sensitivity, and precision. For the classification of MF composition, we used as validation metrics the precision and the recall.

6.3. Integrating pore geometrical features to characterize MFs

To validate the proposed approach, the encoder input images of size 128×128. Each convolutional layer uses a 3×3 kernel, ReLU activation, he_normal initialization. The first three layers have 64, 32, and 16 filters, respectively, each followed by a MaxPooling2D operation with a 2×2 pool size and Batch Normalization. A fourth convolutional layer with 8 filters processes the output, which is then flattened. The resulting features are mapped into two

dense layers to estimate the latent space parameters $[\mu, \sigma]$, both of equal dimensions. A latent vector z is sampled using the reparametrization that combines both $[\mu]$ and $[\sigma]$ by a linear combination, as $z = \mu + \sigma \cdot \epsilon$, where $\epsilon \in \mathcal{N}(0, 1)$.

The decoder reconstructs images from the latent space, beginning with a dense layer that maps the latent vector z to a feature vector with dimensions $16 \times 16 \times 128$, using ReLU activation. The reconstruction process continues with a sequence of convolutional and upsampling layers, using 32, 16, and 8 filters, each accompanied by upsampling layers and batch normalization. The fifth convolutional layer reduces the feature maps to 4 filters, while the last layer uses a single filter with sigmoid activation to generate the reconstructed image of 128×128.

The regressor module is designed to predict scalars, following a sequence of convolutional layers (128, 64, 16 and 8 filters) followed by dense layers for regression. The regressor module outputs these four predictions simultaneously, namely, mean pore area, mean pore perimeter, mean pore equivalent diameter and number of pores. The discriminator convolutional module uses 3 CNN layers with 128,64,16 filters, respectively. The complete architecture was adjusted with an Adam optimizer was implemented with a learning rate of $1 \times 10^{-}6$, during 2000 epochs, and a batch size of 16 images, using 80% of data for training and 20% for testing.

7. EVALUATION AND RESULTS

This research was conducted from two distinct perspectives: the automatic characterization of pore shapes in MFs using U-Net architecture and the integration of the retrieved pore geometrical features into a VAE training scheme to disentangle the obtained latent space. The results obtained from each perspective are presented below:

7.1. Pore Shape Characterization of MFs

7.1.1. Pore segmentation from MFs' micrographs In this work, an automatic pore segmentation was achieved from $\mathbf{X}$ micrograph images. Following, a cross-five fold validation, the adjusted U-net strategy achieved a global dice score of 0.94 ± 0.011. This result evidenced the capability of overlapping pores concerning the expert reference. Also, in such experiments, the adjusted U-net achieved 0.95 ± 0.04 and 0.93 ± 0.010 of sensitivity and specificity, respectively. Some examples of these masks obtained by the U-net model and the automatic quantification of their pore size distribution are shown in Figure 7. As observed, there exists a robust and effective segmentation of pores, allowing the subsequent shape analysis of feature distributions. The right panel of Figure 7 shows the pore size distribution per MF's micrograph, computed from automatic segmentation, which again supports the appropriate results of automatic pore masks.

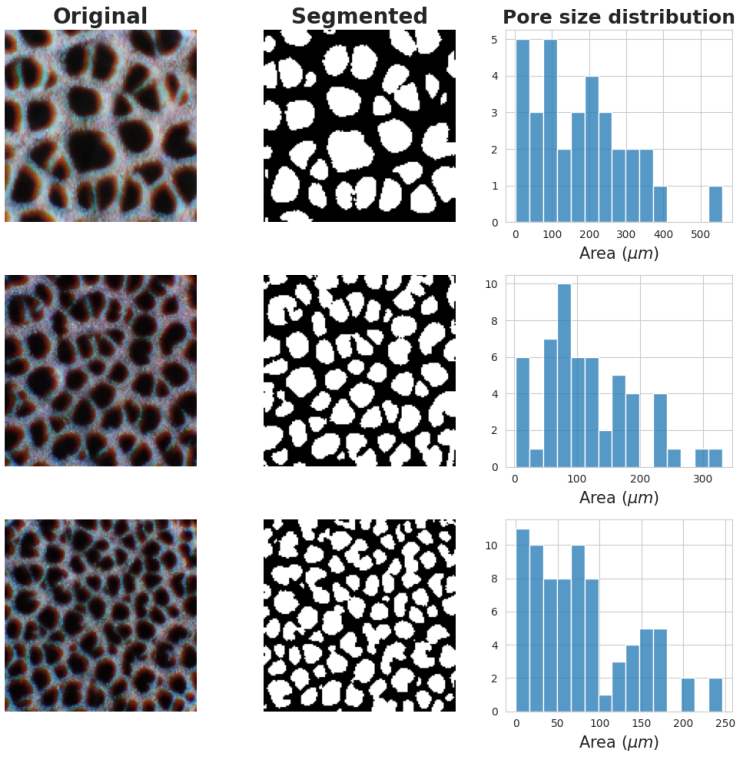

Figure 7. Typical examples of the pore segmentation task achieved by the proposed U-net model. The automatic pore size quantification is also shown for each segmented image.

As an extra evaluation, Table 1 summarizes the comparison of the proposed approach with respect to classical image analysis approximations. As expected, the proposed approach achieved a remarked segmentation capability, learning pore variations, being robust to textural, geometrical and luminance changes of input samples. In fact, a simple threshold is not sufficient to bound pores and therefore is not possible to follow a geometric characterization. In same way, the Otsu approximation reports limitations with overlapping differences of around 30%, which may be crucial to a correct analysis of foams.

Table 1. Segmentation metrics comparison among traditional thresholding and Otsu method against the proposed approach.

Methods	**Dice Score** $\uparrow$	**AVD** $\downarrow$	**Time(ms)** $\downarrow$
Thresholding	0.07 ± 0.01	0.43 ± 0.2	0.42 ± 0.05
Otsu	0.72 ± 0.08	1.98 ± 0.01	0.07 ± 0.01
Proposed Approach	0.91 ± 0.02	0.13 ± 0.05	14 ± 1.2

In contrast, the proposed approach is able to learn intricate and variable patterns within the image data, providing more accurate segmentation even for complex, irregular pore structures. Regarding time processing, the proposed approach take considerable more time (around of 14 ms) but guaranteeing robust pores segmentation. In fact, for a metallic foam (45 images in average) the proposed approach take around of 0.63 seconds, which is feasible solution to carry out a geometric analysis. Figure 8 shows some example of pore segmentation from these approaches.

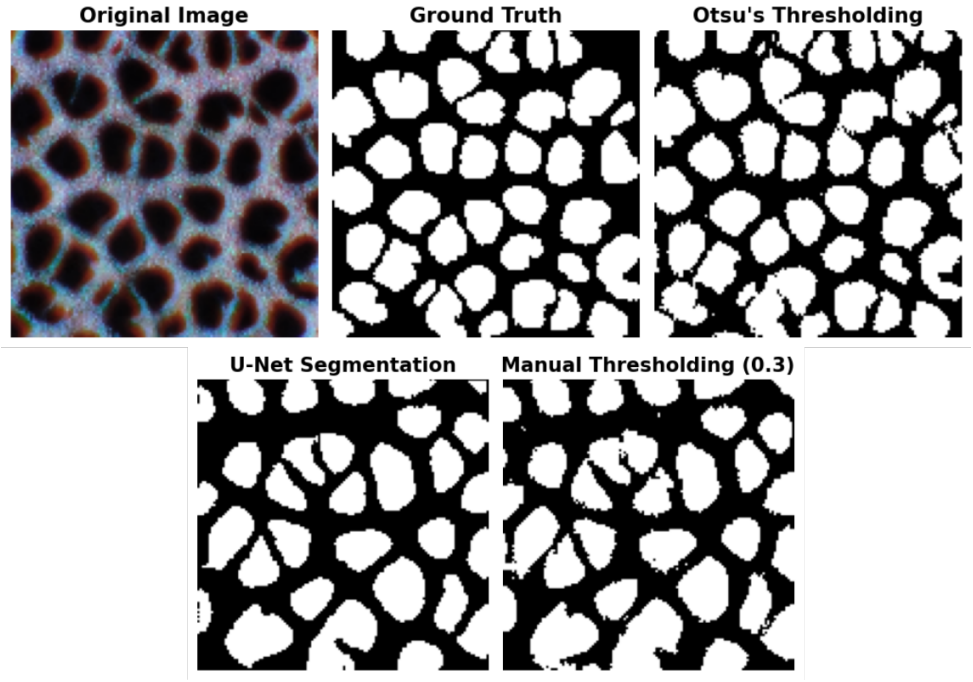

Figure 8. Segmentation results for U-Net model, Otsu and manual thresholding methods compared to the ground truth and original MFs metallic foam.

From retrieved segmentation masks, it was possible to determine geometrical variables clustered according to each composition group of MFs. Table 2 reports the mean (μ) and the standard deviation (σ) of geometrical features for MF1, MF2, and MF3, respectively. As expected, we can observe that simple features, computed globally from first statistical moments can be determinant to differentiate MFs according to their composition.

Table 2. Segmented images' statistical descriptors of the mean (μ) and standard deviation (σ) pore feature values per group of MFs.

Class	Area (μm^2)		Perimeter (μm)		Diamater (μm)		Number of pores	
	μ	σ	μ	σ	μ	σ	μ	σ
MF1	222.20	37.5	60.98	6.83	7.53	0.73	30.18	3.91
MF2	154.71	22.28	51.85	4.51	6.39	0.49	44.41	6.07
MF3	92.99	17.85	41.41	5.28	4.89	0.49	71.81	9.81

7.1.2. Statistical pore distribution and MFs classification In a second validation of the proposed approach, we measure the capability to separate MF composition from geometrical features. Initially, we recover and compute the distribution for each computed feature, and cluster the measures regarding each MF class. Figure 9 summarizes the boxplots for each MF class regarding each geometrical feature computed. Subsequently, we measure statistical differences among these groups using the Kolmogorov-Smirnov (KS) test. Significant differences were observed across all distributions, highlighting the capabilities of automatic analysis to support MF analysis regarding pore geometrical features.

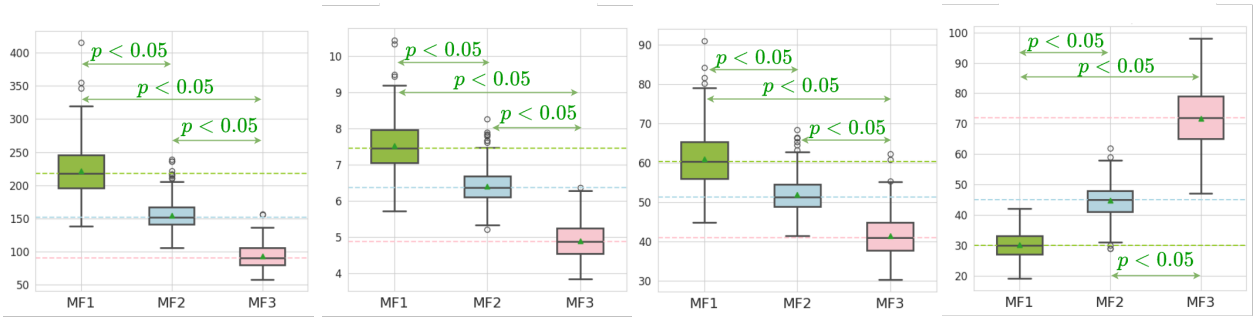

(a) Area (μm) **(b)** Diameter (μm) **(c)** Perimeter (μm) **(d)** Number of pores

Figure 9. Distribution of pore feature values across the three MF classes.

Based on the computed distributions for each micrograph, we performed a classification analysis to evaluate the ability of geometrical features to determine the MF composition class automatically. Table 3 shows the results of the classification task achieved for each

geometrical feature independently. MFs can be easily classified according to their chemical composition using a simple projection of the computed distributions for each MF class. The number of pores is the key geometrical feature supporting this classification, with average precision and recall scores of 92% and 94%, respectively.

Table 3. Classifiers results for PDF using mean pore geometrical features retrieved from MF's micrographs. Pore area and number of pore achieve the best performance at classification new MFs samples.

Class	Area		Perimeter		Equivalent diameter		Number of pores	
	Precision	**Recall**	**Precision**	**Recall**	**Precision**	**Recall**	**Precision**	**Recall**
MF1	0.92 ± 0.03	0.88 ± 0.03	0.85 ± 0.04	0.82 ± 0.03	0.89 ± 0.04	0.82 ± 0.03	0.95 ± 0.01	0.95 ± 0.02
MF2	0.79 ± 0.05	0.83 ± 0.04	0.65 ± 0.04	0.70 ± 0.06	0.73 ± 0.04	0.80 ± 0.06	0.91 ± 0.04	0.90 ± 0.02
MF3	0.94 ± 0.02	0.93 ± 0.04	0.86 ± 0.02	0.88 ± 0.04	0.93 ± 0.03	0.93 ± 0.04	0.96 ± 0.02	0.98 ± 0.03

In a second classification analysis, we use all geometrical features as descriptors and train standard machine learning models, including decision tree (DT), random forest (RF), and support vector machine (SVM). In such cases, the descriptor is conformed by the geometrical features. The resultant descriptors from training images are used to adjust the machine-learning models. Test images, at each fold, are used to compute descriptors and evaluate the performance of trained models. Each model was then adjusted to classify MF samples based on their chemical composition using statistical pore feature descriptors. Table 4 presents the classification results obtained with these methods. As expected, the geometrical descriptor achieved remarkable classification with different strategies, evidencing the robustness of representation from the set of geometrical features. The best score was achieved using an SVM with an average of precision and recall of 0.99 ± 0.01 for the MF3 and the MF1 classes, respectively.

Table 4. Machine learning models result for MF classification using pore features descriptors.

Class	Decision Tree			Random Forest			SVM		
	Precision	**Recall**	**F1-score**	**Precision**	**Recall**	**F1-score**	**Precision**	**Recall**	**F1-score**
MF1	0.93	0.93	0.93	1.00	1.00	1.00	1.00	0.86	0.92
MF2	0.83	0.91	0.87	0.92	1.00	0.96	0.85	1.00	0.92
MF3	1.00	0.91	0.95	1.00	0.91	0.95	1.00	1.00	1.00

7.1.3. Feature important analysis Complementary, a feature importance analysis was conducted to determine which geometrical features best support the characterization of MF samples. To achieve this, we use two approaches: identifying features that enhance machine learning classifiers and performing a correlation analysis of the features. Regarding the importance of machine learning, tree-based and random forest classifiers were used to identify the most influential features for discriminating MF classes. These models identify the most influential features based on their contribution to reducing classification impurity, following an entropy-based principle: features with lower impurity are deemed more important. Additionally, we utilized SVMs to analyze feature importance. SVMs prioritize features that maximize the separation between classes, thus aiding in accurate classification. Figure 10 summarizes the feature importance analysis from the machine learning algorithms. As observed, the number of pores is consistently one of the most relevant features across all three algorithms. Also, pore diameter statistics are relevant for MF discrimination, being the most significant feature in the SVM model.

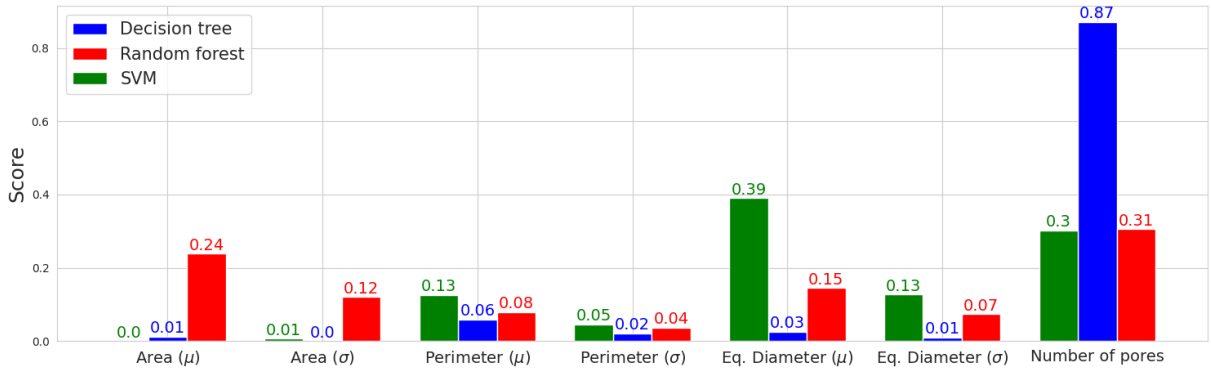

Figure 10. Feature importance results for tree-based machine learning models. The number of pores exhibits the most influential feature for both random forest and decision tree models, highlighting its significance in the classification task.

Additionally, a linear analysis was conducted to measure the correlation among geometric features and their relation to MF composition classes. Figure 11 summarizes the achieved correlations of all considered variables, where extreme positive or negative values indicate a strong dependency between two variables (shown in red colors). As expected, the geometrical features share correlative dependency, standing out the quantitative measure between the area and the number of pores, but also between the area and the boundaries of pores. Notably, the area and number of pores exhibit a significant positive correlation, as do the area and pore boundaries. Interestingly, the correlation analysis confirms the number of pores as an essential feature for understanding material composition, exhibiting a strong correlation with the MF class. Furthermore, the area and diameter statistics also demonstrate linear dependencies that support material classification.

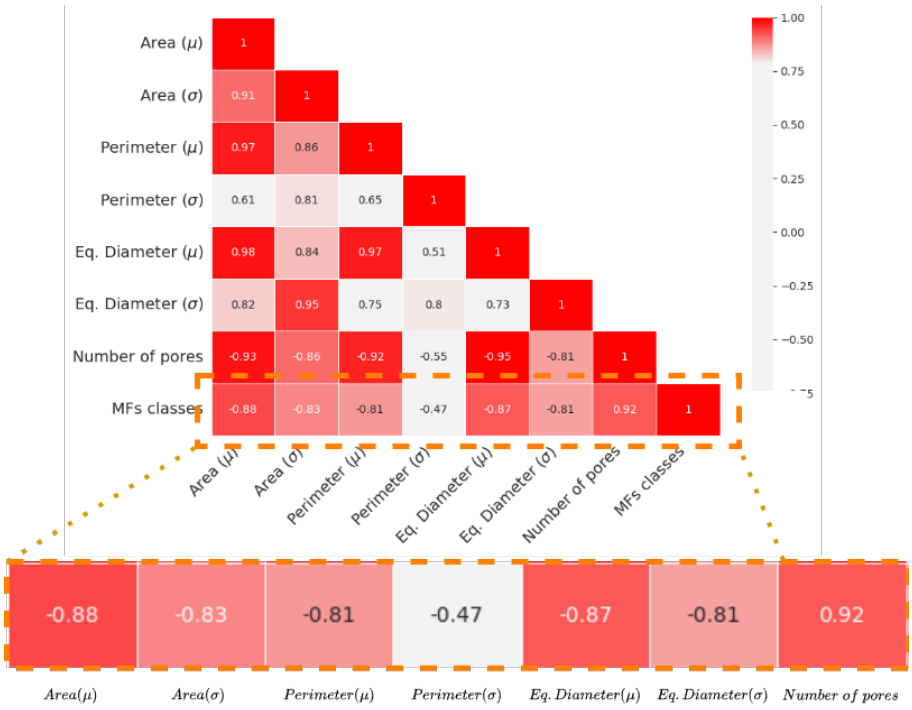

Figure 11. Linear correlations among statistical descriptors of pore features. The number of pores is inversely correlated with the area, perimeter, and diameter of the pores.

The Cu/Ni ratio in bimetallic foams prepared via the DHBT method influences their morphology. Nickel, being more electrochemically active than copper, increases the nucleation rate of hydrogen bubbles[40]. This leads to a higher pore density and smaller average pore size. Conversely, copper, being less electrochemically active, decreases the nucleation rate, which can result in larger pores and lower pore density. In addition to these effects, morphology is another key feature influenced by chemical composition. The presence of nickel tends to promote the formation of more rounded pores[41] whereas copper favors more irregularly shaped

[40] Yuxi CHEN et al. “Magnetic field-controlled bubble templated CuNi foam films and their performance towards hydrogen evolution reaction in alkaline media”. In: *International Journal of Hydrogen Energy* 59 (2024), pp. 625–634.

[41] KI SIWEK et al. “3D nickel foams with controlled morphologies for hydrogen evolution reaction in highly alkaline media”. In: *International journal of hydrogen energy* 44.3 (2019), pp. 1701–1709.

pores[42]. Therefore, it is likely that the number of pores would remain the most important characteristic, even if the Cu/Ni ratio were significantly altered.

7.1.4. Image analysis of porous metallic foams for mercury removal assessment Upon contact with a copper surface, dissolved mercury ions (Hg^{2+}) undergo reduction to form metallic mercury (Hg), producing a copper-mercury amalgam [43]. This amalgamation process, facilitated by our porous metallic foams, leads to mercury removal from aqueous solutions. Copper-nickel alloy amalgamation leads to a thickening of the foam walls. As observed in Figure 12, amalgamation results in a decrease in pore size. A strong correlation between the percentage of mercury removal, as measured by atomic absorption spectroscopy, and the reduction in pore diameter is observed. This indicates that image analysis can serve as a valuable tool for monitoring the extent of mercury removal using metallic foams (MFs). The efficiency of $Hg^{2}+$ removal is influenced by pore size: larger pore diameters enhance removal efficiency. However, increasing the number of pores weakens the mechanical strength of the foams, as thinner foam walls result, making it inadvisable to increase the nickel content.

---

[42] Ying LI et al. "Superhydrophobicity of 3D porous copper films prepared using the hydrogen bubble dynamic template". In: *Chemistry of Materials* 19.23 (2007), pp. 5758–5764.

[43] Mattias K. O. BENGTSSON; Cristian TUNSU, and Björn WICKMAN. "Decontamination of Mercury-Containing Aqueous Streams by Electrochemical Alloy Formation on Copper". In: *Industrial & Engineering Chemistry Research* 58.21 (2019), pp. 9166–9172. DOI: 10.1021/acs.iecr.9b01513.

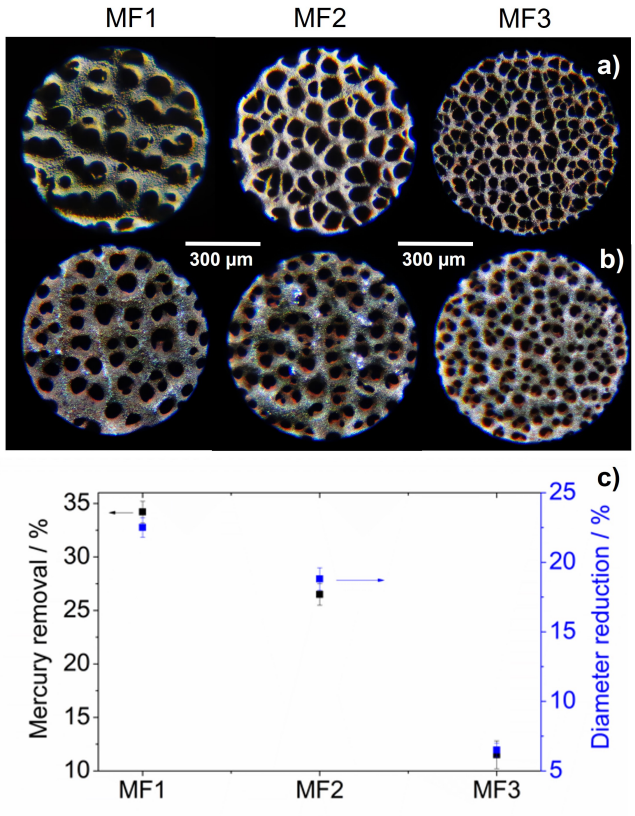

Figure 12. Optical images of metallic foams (MFs): a) pristine, and b) after Hg removal. c) Percentage of Hg^{2+} removed, analyzed using an atomic absorption spectrophotometer, and by the reduction of pore diameter in the MFs. The labels of the MFs are indicated in the figure.

7.2. Integration of Pore Features for MF Characterization

Here, we measure the capability to discriminate MFs classes by projecting embeddings to standard classifiers, such as: K-Nearest Neighbors (KNN), Random Forest, and Decision Trees. The first evaluation involved testing different sizes of the latent vectors: 16, 32, 64, and 128 scalar values. These models differentiate between MFs using the representations of mean (μ), variance (σ), and latent vector (z), obtained from the VAE. Table 5 summarizes the classification results for the embeddings generated by the proposed variational Autoencoder. The findings highlight the model's capacity to represent MFs effectively by leveraging structural features in the latent space.

Table 5. Machine learning models applied to classify embedded vectors produced by various VAE architectures with different latent dimension sizes. Here, μ represents the mean vector, σ denotes the variance vector, and z is the linear combination of both. These vectors, generated by the VAE encoder, are evaluated based on their classification accuracy.

Approach	16			32			64			128		
	μ	σ	**z**	μ	σ	**z**	μ	σ	**z**	μ	σ	**z**
Decision Trees	0,81	0,61	0,81	0,72	0,56	0,71	0,66	0,51	0,65	0,62	0,54	0,60
Random Forest	0,92	0,72	0,92	0,91	0,71	0,90	0,86	0,67	0,85	0,87	0,66	0,86
KNN	0,87	0,68	0,86	0,71	0,61	0,72	0,51	0,47	0,51	0,41	0,35	0,40

The highest classification accuracy was achieved using the 16-dimensional embedded vectors of the mean (μ) and the sampling vector (z) with the random forest classifier. This suggests that class distributions can be effectively differentiated by their mean values, while the dispersion of the distributions is less significant for this task. Additionally, an inverse relationship was observed between the embedding size and the model's ability to distinguish between MF classes, indicating that larger embeddings have sparse descriptors that limit the classification performance. An additional ablation study was conducted by training configurations using only a VAE architecture, and a strategy without the adversarial discriminator. Table 6 presents the classification accuracy results for the three VAE configurations, using a 16-dimensional latent vector. The results indicate that the σ vector is not particularly informative for characterizing the MFs. In contrast, the random forest classifier exhibited the highest performance when classifying the z vector. As observed, each component has a contribution on final discriminative space, achieving a gain of 3.4% regarding VAE+REG, and 19.2% regarding the use of only a VAE strategy.

Table 6. Comparison of accuracy during classification of the latent vectors generated by traditional VAE, VAE plus regressor and discriminative modules (VAE + REG + DISC), and VAE without discriminative module (VAE + REG) using three traditional machine learning approaches

Approach	VAE			VAE + REG			VAE + REG + DISC		
	μ	σ	**z**	μ	σ	**z**	μ	σ	**z**
Decision Trees	0.62	0.56	0.60	0.74	0.59	0.74	**0.81**	0.61	0.81
Random Forest	0.73	0.68	0.70	0.90	0.70	0.88	**0.93**	0.72	0.92
KNN	0.61	0.58	0.59	0.83	0.61	0.82	**0.87**	0.68	0.86

To complement the analysis, precision, and recall metrics were calculated for each class of MFs across all VAE configurations. Table 7 presents the detailed classification per class, following an ablation study with several configurations of the proposed strategy.

Table 7. Classification report of latent vector z per classes using the Random Forest Classifier.

CLASSES	VAE		VAE + REG		VAE + REG + DISC	
	PRECISION	RECALL	PRECISION	RECALL	PRECISION	RECALL
MF1	0,78	0,71	0,91	0,85	0,85	0,97
MF2	0,62	0,59	0,83	0,77	0,76	0,62
MF3	0,89	0,46	0,98	0,92	0,93	0,81

The VAE + REG configuration sufficiently recovered a discriminatory embedding space, especially for the MF2 and MF3 classes. In such a case, the discriminator enhancement can be associated with optimizing the final image reconstruction rather than providing additional support in disentangling the embedding space.

In a subsequent analysis, we select the 16-dimensional embedding representation to observe the geometrical and topological structure, projecting vectors into a lower-dimensional space using Principal Component Analysis (PCA) (see in Figure 13). We decided to project embedding space from three different configurations, following the previous ablation study, using the only VAE autoencoder, aggregating the regression component, and a full architecture with the addition of a discriminator component.

Table 8. Clustering metrics comparison for the VAE, VAE plus regressor, and the VAE+REG+DISC. This comparison was carried out using the 16-dimensional latent vectors, and the low-dimensional representation of these vectors generated by the PCA. As can be observed, in almost the three metrics and both dimensions proposed VAE exceeds the clustering capability of the others architectures, achieving the lowest Davies-Bouldin index (DBI), and higher Silhouette coefficient (SC) and Calinski-Harabasz index (CHI)

CLUSTERING	VAE		VAE + REG		PROPOSED VAE	
METRIC	PCA	Embedding	PCA	Embedding	PCA	Embedding
DBI $\downarrow$	3,88	4,76	1,2	2,95	1,09	2,67
SC $\uparrow$	0,085	0,04	0,25	0,06	0,26	0,06
CHI $\uparrow$	42,56	29,6	114,8	24,9	134,04	28,8

Table 8 summarizes the discrimination capability (following DBI, SC, and CHI metrics) of the embedding space in both configurations: using the original 16-dimensional space and over the two-dimensional PCA space. Notably, the architecture that includes the regressor and the discriminatory component achieved the best DBI (1.09) and SC (0.26) and CHI (134.04) values. In fact, there is a gain of disentangling in about 71.91% and 67.23%, measuring with DBI and CHI, and regarding the typical VAE architecture. These achieved results are key to emulate new components or material compositions from embedding spaces. Also, it should be noted that a major discrimination capability exists from original space to the associated PCA low-dimensional projection. Such fact could be associated to the linear restrictions applied from reduction strategy.

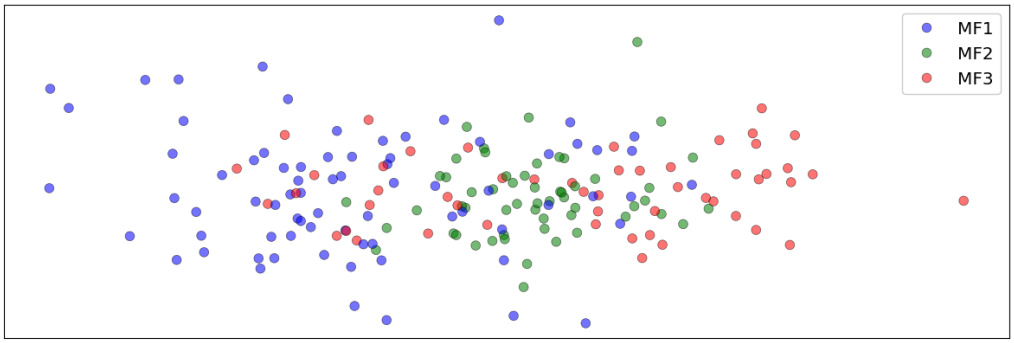

(a) VAE latent space visualization

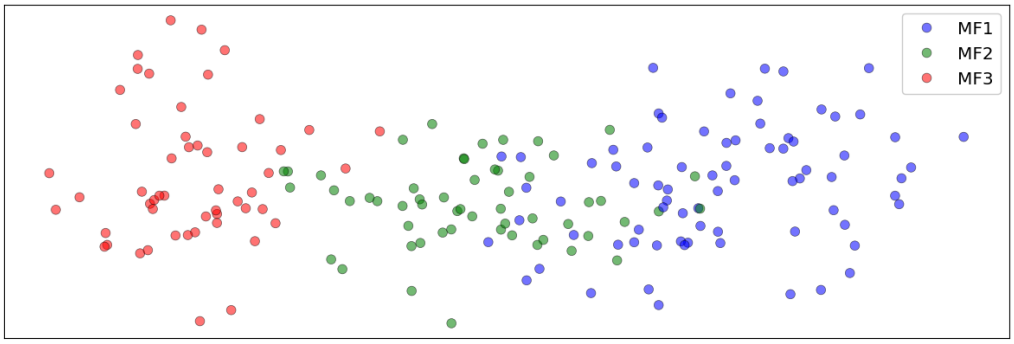

(b) VAE + REG latent space visualization

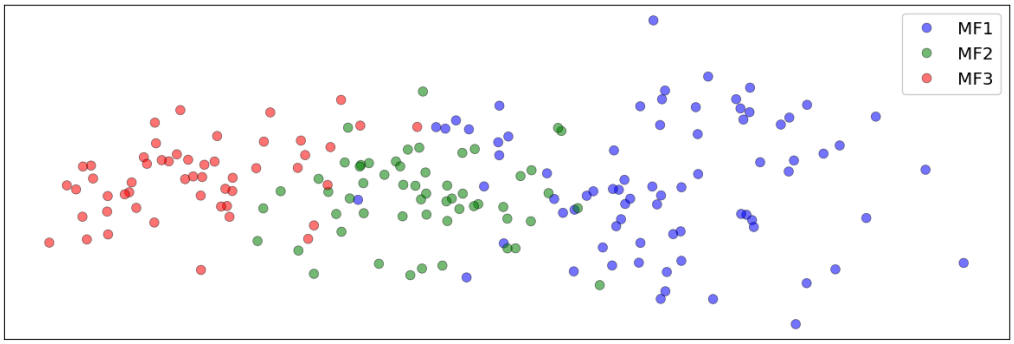

(c) VAE + REG + DISC latent space visualization

Figure 13. Visualization of low-dimensional latent space of embeddings using principal component analysis (PCA)

Figure 13 illustrates the reconstruction of embedding space of each version of the proposed strategy, projecting low-dimension versions into 2D plots. In such a case, it was possible to observe how there exist a major disentanglement capability when the architecture adopts the

regression and discriminator components.

An additional analysis includes projection of the pore features into the embedding space to observe distributions among samples. Figure 14 represents the distribution of the four selected pore characteristics, revealing the correspondence among physical features, which increase from left to right according to MFs classes. As observed, the vectors generated by only the VAE component are entangled among classes, without difficulty separating the vectors. These results highlight the effectiveness of the proposed VAE and the impact of the discriminator module in analyzing MFs' micrographs

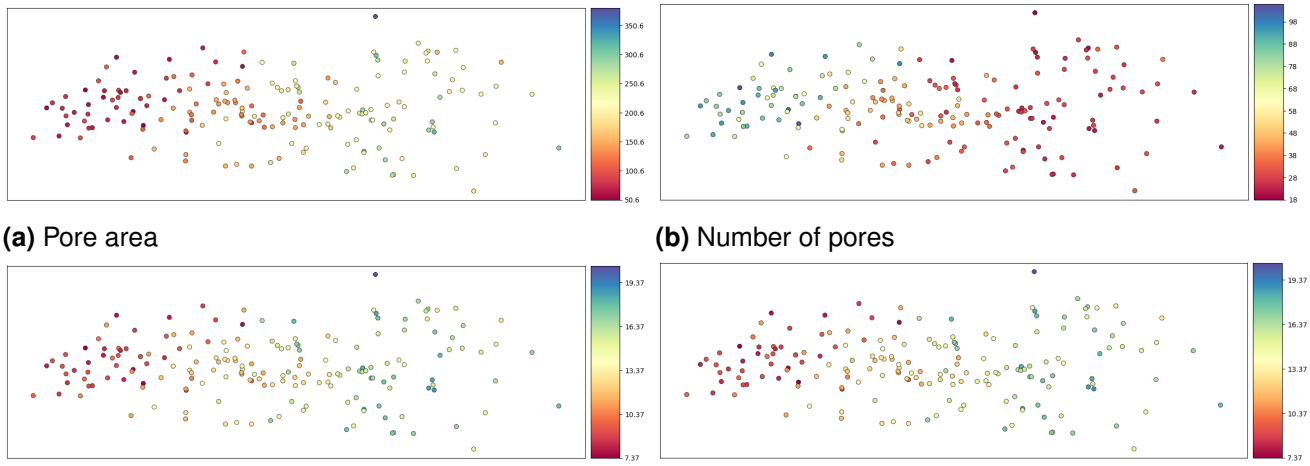

(a) Pore area

(b) Number of pores

(c) Pore equivalent diameter

(d) Pore perimeter

Figure 14. Projection of pore features onto the VAE+REG+DISC's low-dimensional latent space: (a) Pore area, (b) Number of pores, (c) Pore equivalent diameter, and (d) Pore perimeter. The latent space demonstrates a clear disentanglement, where distinct regions correspond to variations in the introduced pore features.

In a final evaluation, Figure 15 shows some retrieved image micrograph reconstructions from the proposed approach. As expected the full proposal achieved better pore reconstruction, achieving major pore resolution from images from 128 dimensional embedding vectors. Despite the remarked reconstruction, it is noteworthy that there exist limitations in the description of interstitial components of the samples.

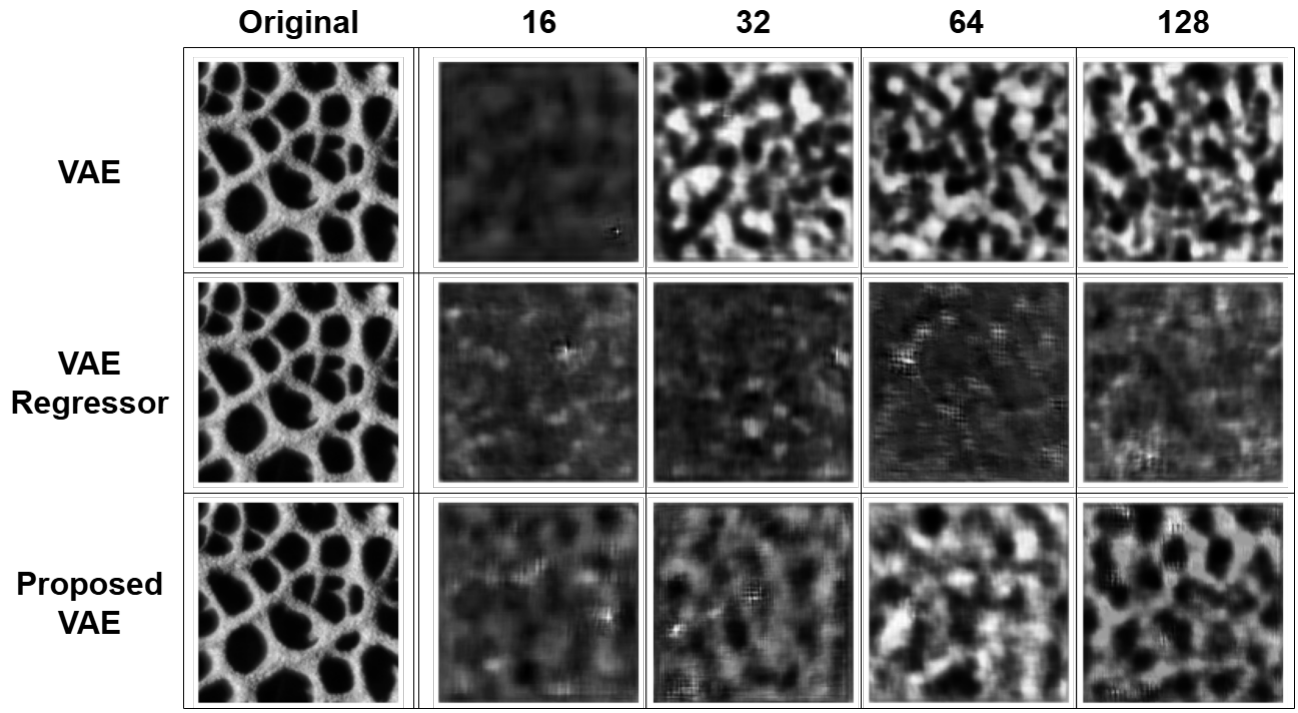

Figure 15. Comparison of reconstructed images from three VAE architectures with different latent dimension sizes, as indicated in the figure.

8. DISCUSSION

This research work introduces two methodologies dedicated to characterize Cu/Ni foams. In this chapter is presented an independent discussion of each approach, introducing the contribution, the evaluation and results and considering other approaches of the state-of-the-art.

8.1. Pore Shape Characterization of MFs

This work presented a computational methodology for the automatic characterization and classification of porous metallic foam compositions. The proposed approach can support the automatic geometric characterization of observed pores in micrograph images. We first developed and adjusted a deep learning architecture dedicated to automatically segmenting pores. In a set of 928 micrograph images, the adjusted method achieved an overlapping score of 0.94 ± 0.04, and a precision of 0.95 ± 0.04, demonstrating efficient performance in automatically delineating pores, even in intricate interstices. Each segmented pore was independently characterized by geometric features, namely: area, perimeter, and diameter, with the number of pores considered as the global reference. These features were used to construct statistical distributions representing the geometric characteristics of each micrograph. These distributions of geometrical features were mapped to machine learning classifiers to obtain an automatic classification of MF compositions. The proposed features achieved a remarkable classification score of 96%, and 85% in precision and recall, respectively. Interestingly, a feature importance analysis revealed that the number of pores and the mean pore area were the most significant features for differentiating MFs based on their composition.
In the literature, various computational approaches exist for automatic support of material

characterization, including pore localization[18] [44] [45]. For instance, Torre et al.[19] fine-tuned Mask R-CNN models using pre-trained weights from the COCO dataset (a dataset of conventional images) to detect and bound pores in SEM images of four different polymeric materials, each with distinct microstructure. In this approach, pores were manually contoured for accurate labeling, achieving a mean average precision (mAP) between 0.27 and 0.33 across 1000 images. Some limitations noted, particularly in missed segmentation for certain pores. Similarly, Zhou et al. used the DeepLabV3+ model, based on the Xception architecture, primarily for segmenting large pores in concrete. This architecture employs an encoder-decoder strategy to analyze pore size distribution in SEM images and demonstrated rapid processing, taking just half an hour for the entire dataset of 1000 images. Also, Karaca's[20] Pore D2 model, built on the YOLOv5 architecture, offers faster dataset processing through an object detection scheme. Despite the strong results, these methodologies rely on coarse segmentation to achieve adequate localization scores. As a result, they may lose pixel-level accuracy, which is important for requiring complete geometric characterization of pores, particularly smaller or more complex pore structures. In contrast, the proposed approach is optimized for full segmentation tasks, preserving fine details of pore boundaries. Moreover, it is trained specifically on metallic foam micrographs, without relying on pretrained weights from unrelated datasets.

The proposed approach also demonstrated superior performance compared to classical image analysis techniques. Simple thresholding was insufficient to capture pore variability, failing to produce accurate segmentation. The Otsu approximation was more competitive in pore segmentation, achieving a Dice score of 72%. Nonetheless, for detailed characterization of different configurations of Cu/Ni metallic foam micrographs, these scores may lack

---

[44] Lucas von CHAMIER et al. "Democratising deep learning for microscopy with ZeroCostDL4Mic". In: *Nature communications* 12.1 (2021), p. 2276.

[45] Aagam SHAH et al. "Automated image segmentation of scanning electron microscopy images of graphene using U-Net Neural Network". In: *Materials Today Communications* 35 (2023), p. 106127.

the sensitivity needed to distinguish between classes. Unlike conventional methods, the proposed approach accounts for pore variability, enabling precise identification of intricate and irregular pore geometries in metallic foams. In fact, it achieved an average Dice score of 91%. Although the method is tailored for metallic foams, simple transfer learning with other foams may be sufficient to extend its applicability to other materials.

The proposed methodology not only provides comprehensive analysis but also optimizes processing time and provides quantitative support for expert evaluation. Future work includes include the incorporation of complementary information, such as mechanical and electrochemical properties, to further enhance the understanding of macro-micro correlations in porous metallic foams. In addition, the tool is expected to be validated on a larger cohort of images, including new material class configurations. The approach is based on a deep earning model specifically designed to recognize pore patterns from Cu/Ni foam observations. Hence, the study and its reported results are limited to Cu/Ni foams. Immediate application to other foams may result in noisy segmentation and errors in geometric analysis, given the strong dependence on pore segmentation. Nonetheless, this computational approach, using a transfer learning strategy, could be adapted to other types of foams, such as ceramics, polymers, or metallic foams (e.g., Al-based, Ti-based). Transfer learning, for a new set of specific observations, adapts the deep model by retaining general porous features while capturing material-specific characteristics. Therefore, an additional perspective for this work is to validate the proposed approach on a larger cohort of images, including new material configurations.

8.2. Integration of Pore Features for MF Characterization

This work introduced a novel computational approach that learns embedded descriptors to represent metallic foams, disentangling their representation based on geometrical features. The proposed approach is a promising alternative to support the design and evaluation of new foam compositions. The proposed approach was based on the learning of hidden Gaus-

sian patterns, from a VAE, which in turn was adjusted from a task dedicated to reconstruct micrographs images. The proposed approach adds a decoder module with information about geometrical pore estimations into the latent space and a module dedicated to reconstruction learning.

In a dataset of 928 micrographs representing three distinct classes of MFs, our proposed module significantly enhanced the model's ability to reconstruct visual pore structures, achieving precision and recall rates of 94% and 84% respectively. Additionally, the proposed VAE demonstrated superior clustering performance compared to traditional VAE, evidenced by achieving the lowest DBI (1.09) and the highest SC (0.26) and CHI (134.04). These improvements were observed in both the 16-dimensional latent space and its 2D low-dimensional representations, with the latter showing notable gains in clustering metrics. These findings support that the use of complementary knowledge (geometrical features in this case) may be key to designing more robust material descriptors, which can be useful for digital interpolation among MFs compositions.

In the literature approaches have been reported to characterize porous materials using data-driven techniques. For example, Zhu et al. proposed a convolutional residual generative framework to optimize surface textures, enhancing tribological performance using 2D sliding surface data from finite element simulations [22]. Their model generated surface patterns that significantly reduced friction coefficients by up to 49% and increased carrying capacity by up to 144%. However, the synthesis process highly depends on random Monte Carlo simulations, which can limit control for the design of new materials. Also, Gómez-Bombarelli et al. incorporated a regressor module within a variational autoencoder (VAE) framework to encode specific features into the latent space, facilitating the embedding of tailored characteristics into generative models [24]. Similarly, in the domain of metallic foams, a VAE was employed to encode confocal microscopic images, characterizing three types of metallic foams (MFs) by

learning embedded descriptors through deep autoencoders [46]. These approaches have evidenced capabilities to code observed images but resultant low-dimensional spaces can be overlapped among embeddings with different geometrical properties of features of interest during the simulations.

The proposed approach leverages the latent space of a VAE to effectively capture and predict key geometric features of metallic foams, enabling the inverse design of foams with specific characteristics, such as pore area, perimeter, aspect ratio, and pore count. By evenly distributing these features across the latent space, the method facilitates clear differentiation among the three classes of metallic foams. For instance, samples with higher pore counts are mapped to one region, while those with larger pore sizes are located in another, demonstrating the model's ability to organize and represent foam designs based on their geometric properties.

This capability underscores the VAE's potential for generating new foam samples with tailored properties that align with existing material classifications. While the method has shown promising results for modeling Cu/Ni metallic foams, its application to other types of foams or porous materials would require additional training and adaptation to specific observations. For example, through a transfer learning strategy, the approach could be extended to ceramic, polymeric, or other metallic foams (e.g., Al-based or Ti-based) by incorporating datasets that reflect their specific pore geometries.

A notable limitation of the current work is the VAE's image reconstruction capability, which may constrain its effectiveness in the inverse design of metallic foams. Future research should focus on enhancing the network's reconstruction performance and validating the approach using larger and more diverse datasets with a wider range of material configurations. Additionally, integrating physical constraints or domain-specific knowledge into the VAE's architecture could improve the interpretability and precision of the generated designs, fur-

---

[46] W.D. ROMERO et al. "Geometrical recognition of metallic foam microstructures using a deep learning approach". In: *Materials Today Communications* 37 (2023). DOI: 10.1016/j.mtcomm.2023.107407.

ther bridging the gap between computational predictions and experimental validation. These advancements will not only improve the robustness of the model but also broaden its applicability, paving the way for innovative material designs across a diverse range of fields.

9. CONCLUSIONS AND FUTURE WORK

This research work presented two computational learning approaches dedicated to characterizing MFs. The first approach segmented pores from micrograph and allowed to quantify automatically geometric features. In the second approach, micrograph observations were integrated with pore geometrical features, forcing disentangling the latent space, and enabling clear differentiation of metallic foams based on both their chemical composition and their pore geometrical features. The proposed solutions support the analysis of MFs, which could potentially be used in the design of new MF compositions. Despite remarkable results, major efforts are demanding on reconstruction of synthesized maps, to exploit the computational synthesis of these structures. Additionally, in the context of this work was constructed a dataset of nanostructured metallic foams (MFs) micrographs with 923 sample images and labels associated to pore shape features such as area, perimeter, equivalent diameter, and the number of pores were extracted for each image. Future works include the analysis with larger datasets, included other compositions of MFs to discover the sensibility of the approach and the capability to project similar pore structural features. In addition, perspectives include the design, coding, and development of new computational mechanisms to enhance the learning of embedding descriptors with the capability to backpropagate to the network and explain from the pore structure of MFs the classification output.

BIBLIOGRAPHY

ALZUBAIDI, Laith et al. “Review of deep learning: concepts, CNN architectures, challenges, applications, future directions”. In: *Journal of big Data* 8 (2021), pp. 1–74 (cit. on p. 18).

ARCHANA, R and JEEVARAJ, PS Eliahim. “Deep learning models for digital image processing: a review”. In: *Artificial Intelligence Review* 57.1 (2024), p. 11 (cit. on p. 19).

ARÉVALO-CID, P; VAZ, MF, and MONTEMOR, MF. “Highly porous FeNi 3D foams produced by one-step electrodeposition: Electrochemical stability and mechanical properties”. In: *Materials Characterization* 193 (2022), p. 112311 (cit. on p. 13).

ARSHAD, Farhan et al. “Bubbles Templated Interconnected Porous Metallic Materials: Synthesis, Surface Modification, and their Electrocatalytic Applications for Water Splitting and Alcohols Oxidation”. In: *ChemistrySelect* 7.41 (2022), e202202774 (cit. on p. 16).

BENGTSSON, Mattias K. O.; TUNSU, Cristian, and WICKMAN, Björn. “Decontamination of Mercury-Containing Aqueous Streams by Electrochemical Alloy Formation on Copper”. In: *Industrial & Engineering Chemistry Research* 58.21 (2019), pp. 9166–9172. DOI: 10.1021/acs.iecr.9b01513 (cit. on p. 49).

BENGTSSON, Mattias KO; TUNSU, Cristian, and WICKMAN, Bjorn. “Decontamination of mercury-containing aqueous streams by electrochemical alloy formation on copper”. In: *Industrial & Engineering Chemistry Research* 58.21 (2019), pp. 9166–9172 (cit. on p. 16).

CHAMIER, Lucas von et al. “Democratising deep learning for microscopy with ZeroCostDL4Mic”. In: *Nature communications* 12.1 (2021), p. 2276 (cit. on p. 58).

CHEN, Yuxi et al. “Magnetic field-controlled bubble templated CuNi foam films and their performance towards hydrogen evolution reaction in alkaline media”. In: *International Journal of Hydrogen Energy* 59 (2024), pp. 625–634 (cit. on p. 48).

CHUNG, Sang Yeop et al. “Pore characteristics and their effects on the material properties of foamed concrete evaluated using micro-CT images and numerical approaches”. In: *Applied Sciences* 7.6 (2017), p. 550 (cit. on p. 21).

DA WANG, Ying et al. “Deep learning in pore scale imaging and modeling”. In: *Earth-Science Reviews* 215 (2021), p. 103555 (cit. on pp. 14, 17, 19).

DAS, Manisha et al. “The versatility of the dynamic hydrogen bubble template derived copper foam on the emerging energy applications: progress and future prospects”. In: *Journal of Materials Chemistry A* 10.26 (2022), pp. 13589–13624 (cit. on p. 16).

DING, Zheng et al. “Guided variational autoencoder for disentanglement learning”. In: *Proceedings of the IEEE/CVF conference on computer vision and pattern recognition*. 2020, pp. 7920–7929 (cit. on p. 20).

DOERSCH, Carl. “Tutorial on variational autoencoders”. In: *arXiv preprint arXiv:1606.05908* (2016) (cit. on p. 32).

GÓMEZ-BOMBARELLI, Rafael et al. “Automatic chemical design using a data-driven continuous representation of molecules”. In: *ACS central science* 4.2 (2018), pp. 268–276 (cit. on pp. 19, 60).

HARKNESS, Rachael et al. “Learning disentangled representations for explainable chest X-ray classification using Dirichlet VAEs”. In: *arXiv preprint arXiv:2302.02979* (2023) (cit. on p. 21).

HILLOULIN, Benoit et al. “Modular deep learning segmentation algorithm for concrete microscopic images”. In: *Construction and Building Materials* 349 (Sept. 2022). DOI: 10.1016/j.conbuildmat.2022.128736 (cit. on pp. 14, 17).

JIAO, Licheng and ZHAO, Jin. “A Survey on the New Generation of Deep Learning in Image Processing”. In: *IEEE Access* 7 (2019), pp. 172231–172263. DOI: 10.1109/ACCESS.2019.2956508 (cit. on p. 31).

KARACA, Ilayda and ALDEMIR DIKICI, Betul. “Quantitative Evaluation of the Pore and Window Sizes of Tissue Engineering Scaffolds on Scanning Electron Microscope Images Using Deep Learning”. In: *ACS Omega* (2024) (cit. on pp. 18, 58).

KHARISSOVA, Oxana Vasilievna; TORRES-MARTÍNEZ, Leticia Myriam, and KHARISOV, Boris Ildusovich. *Handbook of nanomaterials and nanocomposites for energy and environmental applications*. Springer, 2021 (cit. on pp. 13, 14).

KINGMA, Diederik P and WELLING, Max. “Auto-encoding variational bayes”. In: *arXiv preprint arXiv:1312.6114* (2013) (cit. on p. 32).

KINGMA, Diederik P; WELLING, Max, et al. “An introduction to variational autoencoders”. In: *Foundations and Trends® in Machine Learning* 12.4 (2019), pp. 307–392 (cit. on pp. 31, 32).

LI, BQ and LU, X. “The effect of pore structure on the electrical conductivity of Ti”. In: *Transport in Porous Media* 87.1 (2011), pp. 179–189 (cit. on p. 13).

LI, Ying et al. “Superhydrophobicity of 3D porous copper films prepared using the hydrogen bubble dynamic template”. In: *Chemistry of Materials* 19.23 (2007), pp. 5758–5764 (cit. on p. 49).

LIU, Ran and ANTONIOU, Antonia. “A relationship between the geometrical structure of a nanoporous metal foam and its modulus”. In: *Acta Materialia* 61.7 (2013), pp. 2390–2402 (cit. on p. 21).

LIU, Wenqian et al. “Towards visually explaining variational autoencoders”. In: *Proceedings of the IEEE/CVF Conference on Computer Vision and Pattern Recognition*. 2020, pp. 8642–8651 (cit. on p. 20).

LONG, Teng; ZHANG, Yixuan, and ZHANG, Hongbin. “Generative deep learning for the inverse design of materials”. In: *arXiv preprint arXiv:2409.19124* (2024) (cit. on p. 19).

MA, Xurui et al. “Research and development progress of porous foam-based electrodes in advanced electrochemical energy storage devices: A critical review”. In: *Renewable and Sustainable Energy Reviews* 173 (2023), p. 113111 (cit. on pp. 13, 14).

MICHELUCCI, Umberto. “An introduction to autoencoders”. In: *arXiv preprint arXiv:2201.03898* (2022) (cit. on p. 32).

NAM, DoHwan et al. “Effects of (NH4) 2SO4 and BTA on the nanostructure of copper foam prepared by electrodeposition”. In: *Electrochimica Acta* 56.25 (2011), pp. 9397–9405 (cit. on p. 13).

PARK, Yeonjoo and SIMPSON, Douglas G. “Robust probabilistic classification applicable to irregularly sampled functional data”. In: *Computational statistics & data analysis* 131 (2019), pp. 37–49 (cit. on p. 29).

PLOWMAN, Blake J; JONES, Lathe A, and BHARGAVA, Suresh K. “Building with bubbles: the formation of high surface area honeycomb-like films via hydrogen bubble templated electrodeposition”. In: *Chemical Communications* 51.21 (2015), pp. 4331–4346 (cit. on p. 17).

ROMERO, W.D. et al. “Geometrical recognition of metallic foam microstructures using a deep learning approach”. In: *Materials Today Communications* 37 (2023). DOI: 10.1016/j.mtcomm.2023.107407 (cit. on p. 61).

ROMERO, William D et al. “Geometrical Recognition of Metallic Foam Microstructures Using a Deep Learning Approach”. In: *Available at SSRN 4564423* () (cit. on p. 22).

RONNEBERGER, Olaf; FISCHER, Philipp, and BROX, Thomas. “U-net: Convolutional networks for biomedical image segmentation”. In: *Medical Image Computing and Computer-Assisted Intervention–MICCAI 2015: 18th International Conference, Munich, Germany, October 5-9, 2015, Proceedings, Part III 18*. Springer. 2015, pp. 234–241 (cit. on p. 28).

SHAH, Aagam et al. “Automated image segmentation of scanning electron microscopy images of graphene using U-Net Neural Network”. In: *Materials Today Communications* 35 (2023), p. 106127 (cit. on p. 58).

SHIN, H-C; DONG, Jian, and LIU, Meilin. “Nanoporous structures prepared by an electrochemical deposition process”. In: *Advanced Materials* 15.19 (2003), pp. 1610–1614 (cit. on p. 13).

SIWEK, KI et al. “3D nickel foams with controlled morphologies for hydrogen evolution reaction in highly alkaline media”. In: *International journal of hydrogen energy* 44.3 (2019), pp. 1701–1709 (cit. on p. 48).

SURUCU, O. “Electrochemical removal and simultaneous sensing of mercury with inductively coupled plasma-mass spectrometry from drinking water”. In: *Materials Today Chemistry* 23 (2022), p. 100639 (cit. on p. 16).

TORRE, Jorge et al. “On the use of neural networks for the structural characterization of polymeric porous materials”. In: *Polymer* 291 (Jan. 2024). DOI: 10.1016/j.polymer.2023.126597 (cit. on p. 14).

TORRE, Jorge et al. “On the use of neural networks for the structural characterization of polymeric porous materials”. In: *Polymer* 291 (2024), p. 126597 (cit. on pp. 18, 58).

TRAN, Thien-Khanh et al. “Electrochemical treatment of wastewater: Selectivity of the heavy metals removal process”. In: *International Journal of hydrogen energy* 42.45 (2017), pp. 27741–27748 (cit. on p. 16).

VESZTERGOM, Soma et al. “Hydrogen bubble templated metal foams as efficient catalysts of CO2 electroreduction”. In: *ChemCatChem* 13.4 (2021), pp. 1039–1058 (cit. on pp. 14, 16).

VOGELSANGER, Christopher and FEDERAU, Christian. “Latent space analysis of vae and intro-vae applied to 3-dimensional mr brain volumes of multiple sclerosis, leukoencephalopathy, and healthy patients”. In: *arXiv preprint arXiv:2101.06772* (2021) (cit. on p. 33).

WAY, Gregory P and GREENE, Casey S. “Extracting a biologically relevant latent space from cancer transcriptomes with variational autoencoders”. In: *PACIFIC SYMPOSIUM on BIOCOMPUTING 2018: Proceedings of the Pacific Symposium*. World Scientific. 2018, pp. 80–91 (cit. on p. 32).

ZHOU, Shuangxi et al. “Quick image analysis of concrete pore structure based on deep learning”. In: *Construction and Building Materials* 208 (May 2019), pp. 144–157. DOI: 10.1016/J.CONBUILDMAT.2019.03.006 (cit. on pp. 18, 58).

ZHU, Bao et al. “Generative design of texture for sliding surface based on machine learning”. In: *Tribology International* 179 (2023), p. 108139 (cit. on pp. 19, 60).

APPENDICES

Anexo A. Academic Products

Journals

- Romero, W. D., Tami-Pimiento, S., Meléndez, A. M., & Martínez, F. (2025). Deep learning-driven integration of visual and geometric features for automated characterization of nanostructured metallic foams (**Under-review**).
- Romero, W. D., Gutierrez, Y., Tami-Pimiento, L. M., Torres-Bermudez, S., Meléndez, A. M., & Martínez, F. (2024). Automatic pore shape characterization in metal foams templated by hydrogen bubbles from a deep learning strategy. Materials Today Communications, 110937.
- Romero, W. D., Torres-Bermudez, S., Valenzuela, B., Viáfara, C. C., Meléndez, A. M., & Martínez, F. (2023). Geometrical recognition of metallic foam microstructures using a deep learning approach. Materials Today Communications, 37, 107407.